BR

TRI-PP-61
Aug 1990

The Nuclear Response in the $^{54}Fe(\vec{p},\vec{p}')$ Reaction at 290 MeV.

O. Häusser[1,2], M.C. Vetterli[1,2], R.W. Fergerson[3*], C. Glashausser[3], R.G. Jeppesen[1†], R.D. Smith[4], R. Abegg[2], F.T. Baker[5], A. Celler [9], R. L. Helmer [2], R. Henderson[2,6], K. Hicks[2‡], M.J. Iqbal[2], K.P. Jackson [2], K.W. Jones[4], J. Lisantti[7§], J. Mildenberger[1], C.A. Miller[2], R.S. Sawafta[8¶], S. Yen[2]

1) Simon Fraser University, Burnaby, British Columbia, Canada, V5A 1S6.
2) TRIUMF, 4004 Wesbrook Mall, Vancouver, British Columbia, Canada, V6T 2A3.
3) Rutgers University, New Brunswick, NJ 08903, USA.
4) Los Alamos National Laboratory, Los Alamos, NM 87545, USA.
5) University of Georgia, Athens, Georgia 30602, USA.
6) University of Melbourne, Parkville, Victoria, Australia, 3052.
7) University of Oregon, Eugene, OR 97403, USA.
8) University of Alberta, Edmonton, Alberta, Canada, T6G 2N5.
9) University of Western Ontario, London, Ontario, Canada, N6A 3K7.

ABSTRACT

Cross sections, analysing powers and spin-flip probabilities have been measured for inclusive inelastic scattering of 290 MeV protons from ^{54}Fe at laboratory angles between 3.1° and 20°. The momentum transfers vary from small values ($q \sim 0.2$ fm^{-1}) where individual giant resonances of low multipolarity are observed, to larger values ($q \sim 1.4$ fm^{-1}) where quasielastic scattering dominates. Complete measurements of spin observables at 20° are

*Present address: Lockheed Missiles and Space Co., Sunnyvale, CA94089, USA
†Present address: Los Alamos National Laboratory, Los Alamos, NM 87545, USA.
‡Present address: Ohio University, Athens, OH 45701, USA.
§Present address: Indiana University Cyclotron Facility, Bloomington, IN 47405, USA.
¶Present address: Physics Department, Brookhaven National Laboratory, Upton, N.Y. 11973, USA.

TRI-PP 90-61
(9117)

discussed which show that present impulse approximation models based on either the Dirac or the Schrödinger equation for the nucleon are not capable of reproducing all the data. At all momentum and energy transfers the measured analysing powers A_y are smaller than predictions from nonrelativistic calculations. Relativistic calculations explain this reduction of A_y for data near the quasielastic point ($\omega = q^2/2m$) as an effect of the attractive scalar field in the nuclear medium, however they fail to reproduce the observed slopes ($d(A_y)/d\omega$ at fixed angle) assuming for the nuclear response a simple Fermi gas model. For the observed range of momentum and energy transfers ($\omega \leq 96$ MeV at 20°, ≤ 45 MeV at smaller angles) the spin-flip probabilities S_{nn} and spin-flip strengths σS_{nn} appear to be rather insensitive to assumptions about the reaction mechanism and are qualitatively described by a nonrelativistic model of quasielastic scattering which approximates the nuclear response by that of a semi-infinite slab with RPA correlations. Strongly enhanced S_{nn} values are observed for $\omega > 25$ MeV and $q \simeq 100$ MeV/c in agreement with similar observations for several other nuclei. The slab model gives a reasonable account of cross sections and angular distributions for the $^{54}Fe(n,p)^{54}Mn$ reaction at 298 MeV. The inclusion of damping of the response by 2 particle-2 hole excitations and of contributions from two-step processes improves the agreement with the (n,p) data. Using the experimental cross sections for (p,p') and (n,p) reactions and the measured spin-flip strengths in (p,p'), we have separated the nuclear response into spin ($\Delta S = 0$, $\Delta S = 1$), isopin ($T_f = 1,2$) and angular momentum ($L = 0,1,2...$) components. The distribution and strengths of the Gamow Teller, the isovector giant dipole, and the (isoscalar) giant quadrupole resonances have been determined from this analysis and are compared to results from complementary reactions. Relative to quasiparticle RPA calculations the Gamow Teller quenching factors deduced from the σS_{nn} data are slightly smaller than those from (p,n) and (n,p) reactions.

NUCLEAR REACTION: $^{54}Fe(\vec{p},\vec{p}')$, E_p= 290 MeV, cross sections, spin observables.

PACS numbers: 25.40.Ep, 24.50.+g, 24.70.+s, 25.40.-h

(submitted to Physical Review C)

I. INTRODUCTION

Inclusive inelastic nucleon scattering from nuclei at intermediate energies of 200-800 MeV, momentum transfers q = 0 − 3 fm^{-1}, and energy transfers ω = 0 − 100 MeV is of considerable current interest from several perspectives. The data, their theoretical description, and problems in the interpretation, bear strong resemblance to recent studies of inclusive electron scattering [1,2,3]. The results are characterized by the interplay of two distinct features.

At small momentum transfers, q < 1 fm, the energy-loss spectra are dominated by giant resonances of low multipolarity ($L < 4$) which are superimposed on a continuous background. The observation of these resonances, e.g. the analog of the Gamow Teller resonance for (p,p′) (related to the M1 resonance in (e,e′)), and the extraction of their strength provided part of the motivation for the present work. To reduce the model dependence in the separation of giant resonance contributions from the 'background' a large data sample of both cross sections and spin observables was obtained.

At larger momentum transfers the individual giant resonances have died out and it is no longer obvious whether or not the nuclear response plays a major role in the interpretation of the data. The inclusive spectra exhibit a broad peak at energy transfers $\omega \approx q^2/2m$ where m is the nucleon mass. This energy transfer corresponds to the kinematics for NN scattering from a nucleon at rest and the width of the peak may be attributed to Fermi motion of the struck nucleon. The quasifree process can be viewed as the incoherent scattering of the strongly interacting incoming nucleon from nucleons near the nuclear surface. The absence of localized collective giant resonances of low multipolarity whose position and strength depend sensitively on the local nuclear shell structure, and the relative unimportance of Pauli blocking effects make the large-q data suitable to probe the reaction mechanism of NN scattering at nuclear densities. Nonrelativistic calculations for inelastic proton scattering at large q suggest that the (spin) observables for p-nucleus quasifree scattering are appropriate averages of those for free pp and np scattering [4]. Differences between observables and calculations using free NN values may then be ascribed

to modifications of the NN interaction in the nucleus. Such medium effects are implicit in relativistic models of elastic [5,6] and inelastic [7,8] nucleon scattering which postulate an enhancement of the Dirac lower components of the nucleon in the presence of strong and opposing scalar and vector potentials. In the model of Horowitz and Iqbal [7] an effective nucleon mass m* is calculated in an eikonal approximation which turns out to be smaller than the free nucleon mass m because of the attractive scalar potential in the nuclear medium. Experimental support in favor of relativistic effects in quasifree scattering has mainly been confined to data on analysing powers [9,10] or induced polarizations [11,12] which show a reduction compared to the free NN values.

It is an over-simplification to view inclusive quasielastic nucleon scattering data as merely dependent on the NN input and on possible medium modifications. Nuclear many-body correlations may be of comparable importance. The struck nucleon can interact with other target nucleons via the residual particle-hole interaction V_{ph} which can introduce shifts in the quasielastic peak and deviations in the spin observables. At small momentum transfer and low ω the nuclear structure aspects can be incorporated into distorted wave impulse approximation (DWIA) calculations either using a large-basis shell model or the random-phase approximation. At large momentum transfers and high ω these calculations become increasingly cumbersome and less reliable. Approximate methods must be used.

The basic surface character of quasielastic nucleon scattering is contained in the semi-infinite slab model (SISM) of Bertsch, Scholten and Esbensen [13,14]. In this model the N-nucleus cross section is written by a factorized approximation

$$\frac{d^2\sigma}{d\Omega dE} = A_{eff} \sum_{S,T} \frac{k}{k'} tr\{f^{\dagger}_{ST}(\vec{q}) f_{ST}(\vec{q})\} S_{ST}(q,\omega) \qquad (1)$$

The nuclear ground state is assumed to have zero spin and isospin (for ^{54}Fe this is incorrect since T=1), and the sum is over spin S and isospin T transferred to the nucleus. S_{ST} is the nuclear response function which is normalized to unity in the absence of Pauli blocking, and f_{ST} are the corresponding free NN amplitudes. The trace is over both target and projectile spins. The effective number of struck target nucleons, A_{eff}, is the probability, averaged over impact parameters, that the incoming nucleon will interact

with a target nucleon and subsequently escape without absorption. A_{eff} is related to the volume integral of the imaginary optical potential [15] and can thus be determined by elastic scattering experiments. Several important effects on quasielastic (spin) observables have been evaluated recently in the SISM by Smith and collaborators [15,16]. They are, 1) the influence of 2 particle-2 hole (2p2h) correlations on the response function S_{ST}; 2) the contributions from two-step processes; 3) the choice of frame in which to evaluate the NN amplitudes; 4) the effect of optical and spin-orbit distortions.

The large number of effects which are of significance in quasielastic nucleon scattering make it highly desirable to establish a large data base to confront the theoretical models with as many different observables as possible. We report here comprehensive measurements for ^{54}Fe(p, p') at E_p = 290 MeV. Some of these results have been reported previously [9,12]. After a description of the experimental method used to obtain spin observables using the focal plane polarimeter at TRIUMF (section 2) we discuss elastic scattering results which determine distortion effects for the incoming and outgoing protons and which allow us to deduce A_{eff} (section 3). A complete set of eight different observables at $\theta = 20°$ is discussed in section 4. We show that the spin-flip probability is rather insensitive to the reaction model, and that the nuclear response function produces the dominant features in the observed spin-flip probability S_{nn}. In section 5 small-angle (p,p') cross sections, analysing powers and spin-flip probabilities are discussed together with ^{54}Fe(n, p) cross sections [17] in terms of nonrelativistic surface RPA (random phase approximation) calculations. These calculations evaluate the NN amplitudes in the Breit frame; they include 2p2h damping and two-step processes but neglect the effect of spin-orbit distortions. Finally (see section 6) we exploit the well-known property of N-nucleus scattering that different angular momentum transfers L peak at well separated angles. Independent multipole decompositions have been carried out for both the S = 1 and S = 0 strength functions. Estimates of the location and integrated strength of Gamow Teller, of isovector giant dipole, and of (isoscalar) giant quadrupole resonances are presented.

II. EXPERIMENT

The (p, p') experiments were performed in the proton hall at TRIUMF using 290 MeV polarized protons from the TRIUMF cyclotron. A recently implemented configuration of beamline 4B (BL4B) and the installation [18] of two new superconducting solenoids S1 and S2 in the vault section of BL4 made it possible to use longitudinally ($\hat{l}$) polarized beam for the first time. A third solenoid S3 after the last bending magnet was used, without S1 and S2, to precess the proton spin from the normal $\hat{n}$ to the sideways $\hat{s}$ direction. The three components of the incident proton beam were determined using two in-beam polarimeters [19] in separate beamlines (BL4A and BL4B) which differ by a 25° bend. The in-beam polarimeters determine left-right and up-down asymmetries in pp scattering from a CH_2 target at $\theta_{lab} = 17°$ using pairs of plastic scintillator telescopes. After subtracting contributions to the individual coincidence yields from the C(p,2p) reaction the beam polarizations were measured to an accuracy of typically 1% using a value [20] $A_y = 0.405$ for pp scattering at 17° and 290 MeV.

For the $\hat{s}$ measurements the same sideways polarization was obtained by reversing simultaneously the beam polarization at the ion source and the polarity of S3 in BL4B. By averaging pairs of runs with the same sideways polarization P_s the effects of small $\hat{l}$ and $\hat{n}$ polarizations cancel, eliminating the need to know their precise values. In all cases the large component was between 0.70 and 0.77 and the small components were less than 3%.

For small scattering angle measurements the proton beam was dispersed vertically (dispersion = -7cm/%Δp/p) and stopped in a copper block 1.3 m downstream of the target. The target consisted of a 94 mg/cm^2 thick metallic foil isotopically enriched to 98% in ^{54}Fe. Scattered particles were identified and momentum analyzed in the medium-resolution spectrometer (MRS), a 1.4 GeV/c quadrupole-dipole (QD) system with a vertical bend angle of 60° for the central ray. In the dispersion matching mode an energy resolution of about 160 keV was obtained, with a large contribution from energy straggling in the target. At $\theta_{lab} = 20°$ where no sharp features were expected in the missing mass spectrum an achromatic beam with an energy resolution of about 500 keV FWHM was used. For

these measurements the beam was stopped in a shielded beam dump.

A horizontal drift chamber consisting of two (X,Y) pairs of offset planes and located between the target and the MRS QD system, and two pairs of vertical drift chambers near the focal plane were used to trace particle trajectories back to the target. Redundancy in the ray tracing proved essential to eliminate scattered and degraded beam particles. Measurements with (sd)-shell targets which provide (p,p′) spectra with large gaps between levels at low excitation showed [21,22] that instrumental background is negligible at angles as small as 3°. The effective scattering angle was determined to a precision of better than $\pm 0.1°$ using the kinematic crossing of elastic protons from targets of small mass (e.g. H in a CH_2 target) and inelastic protons from targets of larger mass (e.g. the 15.11 MeV state in ^{12}C). Cross sections and analysing powers A_y were measured in overlapping angular steps. These runs were short and separate from those involving the focal plane polarimeter (FPP). In addition to elastic and inelastic data for ^{54}Fe(p, p) the elementary pp reaction was also measured using a CH_2 target. The absolute pp cross sections were typically 6% lower than those predicted by the SP88 phase-shift prediction of Arndt at 290 MeV [20]. The cross sections for ^{54}Fe(p, p′) were scaled upwards by the ratio σ(Arndt)/σ(pp) and a systematic error of $\pm 8\%$ was adopted for the absolute ^{54}Fe cross sections.

The transverse polarizations $P_{n''}$ and $P_{s''}$ of the momentum-analysed protons were measured with the FPP by secondary inclusive scattering in a 7.5 cm thick carbon slab mounted downstream of the focal plane. The components and the properties of the FPP are described in detail elsewhere [23,24]. The position information from 6 pairs of wire chambers is used to reconstruct [26] the direction of the incoming and outgoing proton, the scattering vertex in the carbon slab, and the polar and azimuthal scattering angles θ_c and ϕ_c, respectively. Events with θ_c between 5° and 20° have large analysing powers $A(\theta_c)$ for inclusive proton scattering from carbon. For a momentum bite corresponding to 50 MeV of excitation at E_p = 290 MeV the FPP acceptance does not depend on the azimuthal angle and the transverse proton polarization components are then obtained from [25,26]

$$P_{n''} = 2\frac{\sum_{ev} A(\theta_c)\cos\phi_c}{\sum_{ev} A^2(\theta_c)} \tag{2}$$

$$P_{s''} = -2\frac{\sum_{ev} A(\theta_c)\sin\phi_c}{\sum_{ev} A^2(\theta_c)} \tag{3}$$

with $\phi_c = 0°$ along the dispersion axis.

The statistical errors of the polarizations are given by

$$\delta^2(P_{n''}) = \delta^2(P_{s''}) = \frac{2}{\sum_{ev} A^2(\theta_c)} \tag{4}$$

During the event-by-event replay the quantities $\sum_{ev} A(\theta_c)\cos\phi_c$, $\sum_{ev} A(\theta_c)\sin\phi_c$, and $\sum_{ev} A^2(\theta_c)$ are accumulated and stored in momentum bins of suitable width to allow extraction of the transverse polarizations and of the spin observables (see below). Protons of known transverse polarization at the FPP were produced in ^{208}Pb(p, p) elastic scattering using the identity $P = A_y$. From these measurements the carbon analysing powers $A(\theta_c)$ were determined at energies of 200 and 290 MeV and polar angles $\theta_c = 5 - 20°$ and found [24,26] to be in good agreement with the energy and angle dependence parameterized by Aprile-Giboni *et al.* [27].

In the following we trace briefly the necessary steps to calculate the seven parity-allowed spin observables for inelastic proton scattering from a spin-zero target for the MRS geometry using the measured FPP polarizations. For detailed derivations of the expressions we refer the reader to previous work [28]. We distinguish the proton polarization in three different coordinate systems. The transformation from the helicity frame of the incident beam ($\hat{s} = \hat{n} \times \hat{l}, \hat{n} = \hat{k}_i \times \hat{k}_f, \hat{l} = \hat{k}_i$) to the helicity frame of the protons after the primary scattering ($\hat{s}', \hat{n}', \hat{l}'$), where $\hat{n}' = \hat{n}$, $\hat{l}'$ is along the wave vector $\vec{k_f}$ and $\hat{s}' = \hat{n}' \times \hat{l}'$, is given by

$$\begin{bmatrix} P_{s'} \\ P_{n'} \\ P_{l'} \end{bmatrix} = \left\{ \begin{bmatrix} D_{ss'} & 0 & -D_{ls'} \\ 0 & D_{nn} & 0 \\ D_{sl'} & 0 & D_{ll'} \end{bmatrix} \begin{bmatrix} P_s \\ P_n \\ P_l \end{bmatrix} + \begin{bmatrix} 0 \\ P(\theta) \\ 0 \end{bmatrix} \right\} \frac{1}{1 + P_n A_y} \tag{5}$$

where $P(\theta)$ is the polarization induced by the target, A_y is the vector analyzing power for the reaction, and the spin transfer coefficients D_{nn}, $D_{ll'}$, $D_{ss'}$, $D_{ls'}$, and $D_{sl'}$ correspond to the Wolfenstein parameters D, A′, R, A and R′, respectively.

The magnetic field of the MRS dipole causes the proton spins to precess about the $\hat{s}'$

axis such that the polarization at the focal plane $(\hat{s}'', \hat{n}'', \hat{l}'')$ is given by

$$\begin{bmatrix} P_{s''} \\ P_{n''} \\ P_{l''} \end{bmatrix} = \begin{bmatrix} 1 & 0 & 0 \\ 0 & \cos\chi & \sin\chi \\ 0 & -\sin\chi & \cos\chi \end{bmatrix} \begin{bmatrix} P_{s'} \\ P_{n'} \\ P_{l'} \end{bmatrix} \tag{6}$$

where χ is the Thomas precession angle of the proton spin

$$\chi = \gamma(\mu - 1)\alpha \tag{7}$$

with γ the Lorentz factor and $\mu = 2.792846$ n.m. the proton magnetic moment. The bend angle of the MRS, $\alpha = 60 \pm 1.5°$, is determined for each position along the focal plane by accumulating bend-angle distributions event by event.

The derivation of the spin observables from Equations 2-7 is straightforward. We give the results here for completeness for the three types of incident beam. Since we find that the beam polarization components at the target are reversed within experimental errors when the polarization at the ion source is reversed we need to consider explicitly only a single beam polarization (P_s,P_n,P_l) where the main component is always large and positive. For normal $\hat{n}$ and longitudinal $\hat{l}$ beam, the FPP polarizations $P_{n''}$ and $P_{s''}$ are labelled by the proton polarization at the ion source $j = \{\uparrow, \downarrow\}$. For sideways $\hat{s}$ beam an additional label is needed to distinguish the solenoid polarity $i = \{p, m\}$. Note that $\{ij\} = \{p\uparrow\}$ refers to a beam with positive $P_s \sim 0.75$. Values for the induced polarization P are obtained independently for each of the three beam orientations which can be averaged with appropriate statistical weights to obtain improved accuracy for P. We also quote two check relationships C_{ss} and C_{ns}, which should vanish within statistical errors and which provide useful tests of the reliability of the FPP results.

a) sideways beam, $P_s \gg |P_n|, |P_l|$

$$D_{ss'} = \frac{(1 + P_n A_y)(P_{s''}^{p\uparrow} + P_{s''}^{m\downarrow}) - (1 - P_n A_y)(P_{s''}^{m\uparrow} + P_{s''}^{p\downarrow})}{4P_s} \tag{8}$$

$$D_{sl'} = \frac{(1 + P_n A_y)(P_{n''}^{p\uparrow} + P_{n''}^{m\downarrow}) - (1 - P_n A_y)(P_{n''}^{m\uparrow} + P_{n''}^{p\downarrow}) - 4D_{nn}P_n cos\chi}{4P_s sin\chi} \tag{9}$$

$$P = \frac{(1 + P_n A_y)(P_{n''}^{p\uparrow} + P_{n''}^{m\downarrow}) + (1 - P_n A_y)(P_{n''}^{m\uparrow} + P_{n''}^{p\downarrow})}{4cos\chi} \tag{10}$$

$$C_{ss} = \frac{(1 + P_n A_y)(P_{s''}^{p\uparrow} + P_{s''}^{m\downarrow}) + (1 - P_n A_y)(P_{s''}^{m\uparrow} + P_{s''}^{p\downarrow})}{4} \approx 0 \tag{11}$$

b) normal beam, $P_n \gg |P_s|, |P_l|$

$$D_{nn} = \frac{(1 + P_n A_y)P_{n''}^{\uparrow} - (1 - P_n A_y)P_{n''}^{\downarrow} - 2D_{sl'}P_s sin\chi - 2D_{ll'}P_l sin\chi}{2P_n cos\chi} \tag{12}$$

$$P = \frac{(1 + P_n A_y)P_{n''}^{\uparrow} + (1 - P_n A_y)P_{n''}^{\downarrow}}{2cos\chi} \tag{13}$$

$$C_{ns} = \frac{(1 + P_n A_y)P_{s''}^{\uparrow} + (1 - P_n A_y)P_{s''}^{\downarrow}}{2} \approx 0 \tag{14}$$

c) longitudinal beam, $P_l \gg |P_s|, |P_n|$

$$D_{ll'} = \frac{(1 + P_n A_y)P_{n''}^{\uparrow} - (1 - P_n A_y)P_{n''}^{\downarrow} - 2D_{nn}P_n cos\chi - 2D_{sl'}P_s sin\chi}{2P_l sin\chi} \tag{15}$$

$$D_{ls'} = \frac{(1 + P_n A_y)P_{s''}^{\uparrow} - (1 - P_n A_y)P_{s''}^{\downarrow} - 2D_{ss'}P_s}{2P_l} \tag{16}$$

$$P = \frac{(1 + P_n A_y)P_{n''}^{\uparrow} + (1 - P_n A_y)P_{n''}^{\downarrow}}{2cos\chi} \tag{17}$$

The equations 9, 12, 15 and 16 contain on the right hand side products of D_{ij}'s and small beam polarization components. They can be solved iteratively by initially ignoring these small terms. The spin-flip probability S_{nn} is related to the polarization transfer coefficient D_{nn} by

$$S_{nn} = (1 - D_{nn})/2 \tag{18}$$

III. ELASTIC SCATTERING AND A_{eff}

The cross section for inelastic scattering depends critically on the distortion of the incident and the scattered nucleon. In the surface-peaked reaction the effective number of nucleons participating in a single hard scattering, A_{eff}, can be estimated from the optical distorting potential which can be determined by elastic scattering. In the eikonal limit [4]

$$A_{eff} = \int d^2b\, T(b)\, e^{-\sigma_{NN}T(b)} \tag{19}$$

$$T(b) = \int_{-\infty}^{\infty} dz\ \rho(r), \quad \vec{r} = (\vec{b}, z) \tag{20}$$

The thickness function $T(b)$ is the integral of the nuclear density ρ along the projectile trajectory at impact parameter b. For a short-range NN interaction σ_{NN} is related to the volume integral of the imaginary part of the optical potential $iW(r)$ by [15]

$$\sigma_{NN} = \frac{2m}{Ap} \int d^3r\ W(r) \tag{21}$$

Cross sections and analyzing powers for proton elastic scattering from ^{54}Fe at 290 MeV were measured between $\theta_{lab} = 3 - 50°$. The results are shown in Figure 1 together with fits using two different phenomenological optical models. The solid lines correspond to a relativistic potential with large attractive scalar and repulsive vector potentials [5,6] (see Table I). The dashed lines represent a nonrelativistic potential with standard Woods-Saxon parametrization whose values are shown in Table II. The volume integral of the imaginary part of this potential, $\int d^3r\ W(r)/A = 168\ MeV\ fm^3$, corresponds to an NN cross section $\sigma_{NN} = 20.2$ mb. Since the potential of Table II is not unique we have used other potentials which give acceptable, although slightly worse, fits to the data of Figure 1. With such a potential we obtained $\sigma_{NN} = 23.5$ mb, the difference being larger than the systematic uncertainty of $\pm 8\%$ in the elastic cross sections. The results of SISM calculations presented below assumed a value $\sigma_{NN} = 23$ mb which is within the allowed range of the elastic scattering data. From equation 19 and using $\sigma_{NN} = 23$ mb we calculate $A_{eff}/A = 0.3$ and $A_{eff} = 16$.

IV. COMPLETE (p,p') SPIN OBSERVABLES AT $\theta = 20°$

In this section we discuss the complete set of parity-allowed, independent spin observables for inelastic proton scattering from a spin-zero target; they are A_y, P, $D_{ss'}$, D_{nn}, $D_{ll'}$, $D_{sl'}$ and $D_{ls'}$. The results for 290 MeV, $\theta = 20°$ have been presented briefly before [12]. The results were obtained from the FPP polarization data using equations 2-17 with explicit inclusion in the analysis of the small polarization components of the incident beam. The data encompass energy transfers $\omega = 0 - 90$ MeV with the momentum transfers varying between 272 and 296 MeV/c. By examining in detail this wealth of information one may

hope to identify and separate the effects of medium modifications of the NN interaction and of nuclear many-body correlations. Our analysis is made difficult by the fact that no complete, self-consistent theory has yet been developed which includes all the effects that are known to be important. Therefore it is not possible to examine one particular effect with all the other parameters unchanged. Our conclusions are arrived at by comparing the spin observables separately to relativistic [7,8] and nonrelativistic [13,14,15,16] models. We will show that the most commonly measured observable A_y is strongly dependent on both the reaction mechanism and on the residual interaction V_{ph}. This is in contrast to the spin-flip probability S_{nn} which is least sensitive to assumptions about the reaction mechanism but strongly dependent on the nuclear response function $S_{ST}(q,\omega)$. It is this property which can be exploited to examine the residual interaction in different spin-isospin channels.

Relativistic impulse approximation calculations and medium modifications

Medium modifications of the NN interaction are implicit in relativistic impulse approximation (RIA) models [5,6,7,8] which use Dirac spinors with enhanced lower components. The four-component spinor for the incident proton of momentum $\vec{k}_1$ is

$$U_1(\vec{k}_1) = \left[\frac{E_1^* + m_1^*}{2m_1^*}\right]^{\frac{1}{2}} \begin{bmatrix} 1 \\ \frac{\vec{\sigma}\cdot\vec{k}_1}{E_1^* + m_1^*} \end{bmatrix} \chi_1 \tag{22}$$

where χ_1 is a two-component Pauli spinor and

$$E_1^* = \left(\vec{k}_1^2 + m_1^{*2}\right)^{\frac{1}{2}} \tag{23}$$

The effective mass for the projectile, $m_1^* = m - V_S$, is reduced from the free nucleon mass by the attractive scalar field at nuclear densities. Mean field theory predicts [29] $m^* \approx 0.56\ m$ at central density ρ_o. Since the quasielastic reaction is surface peaked the effective density probed by the projectile is smaller than ρ_o and can be estimated by an eikonal approximation [7,8] which yields $m_1^* = 0.86\ m$ for 290 MeV protons and ^{54}Fe. The struck nucleon is at slightly larger density than the incoming projectile and experiences thus a larger mean field shift, $m_2^* = 0.85\ m$. The relativistic model includes the effects of spin-orbit distortions which turn out to be small. All observables are averaged over a

Fermi gas momentum distribution for the struck nucleons. These momenta $\vec{p}_2$ range up to the Fermi momentum $k_F = 270$ MeV/c.

In Figure 2 the experimental spin observables are compared to the relativistic calculations published previously [12]. The solid lines include the mean field shift of the mass and enhanced lower components whereas the dashed line assumes $m^* = m$. The most striking feature of the data is the variation (mainly a decrease) of the spin observables with increasing ω. This variation is reasonably well reproduced by the calculations for $D_{ss'}$, $D_{ll'}$, and $D_{ls'}$, but not for $(-D_{sl'})$. We understand the slopes in these quantities as a purely kinematic effect. If we denote the momenta of incident and scattered nucleon by $\{\vec{k}_1, \vec{k'}_1\}$ and those of the struck nucleon by $\{\vec{p}_2, \vec{p'}_2\}$ the four-momentum transfer is

$$\omega = E_1^* - E'^*_1 = E'^*_2 - E_2^* \tag{24}$$

$$\vec{q} = \vec{k}_1 - \vec{k'}_1 = \vec{p'}_2 - \vec{p}_2$$

$$q^2 = {k_1}^2 + {k'_1}^2 - 2k_1k'_1 cos\theta_{lab}$$

For each momentum p_2 and azimuthal angle ϕ between $\vec{q}$ and $\vec{p}_2$ the NN amplitudes have to be evaluated at an effective laboratory kinetic energy

$$T_L^{eff} = \frac{s - 4m^2}{2m} = \frac{E_1^* E_2^* - \vec{k}_1 \cdot \vec{p}_2 - m^2}{m} \tag{25}$$

and an effective center-of-momentum scattering angle

$$tan\left(\frac{\theta_{cm}}{2}\right) = \left(1 + \frac{T_L^{eff}}{2m}\right)^{\frac{1}{2}} tan\left(\theta_{lab}\right) \tag{26}$$

As ω varies different target nucleon momenta p_2 and effective laboratory energies T_L^{eff} are sampled. If a particular NN spin observable varies with energy for pp and/or pn scattering the same observable in (p,p') will exhibit a slope versus ω.

From such kinematic considerations one expects little variation with ω for D_{nn}, P and A_y, in obvious conflict with the data. We shall see in the following that the slopes for these observables arise from the residual interaction which is neglected in the simple Fermi gas model assumed in the RIA. Before the relativistic RPA is developed and incorporated

into the RIA the present RIA calculations should be compared to the data only near the quasielastic point $\omega_o = q^2/2m \approx 40$ MeV. We observe that the effect of the enhancement of the lower Dirac component goes in the right direction for every observable with the exception of D_{nn} where there is essentially no relativistic effect. The reduction of P or A_y at the quasielastic point is quantitatively reproduced by the RIA, in agreement with previous observations [9,10,11,12]. This reduction of A_y or P at present cannot be explained by any other mechanism and appears to be a purely relativistic signature. The relative insensitivity of D_{nn} or S_{nn} to Dirac effects validates the nonrelativistic analysis of spin-flip strength presented below.

Nonrelativistic semi-infinite slab model calculations

The surface character of the (p,p') reaction is an essential feature which is not included in the RIA. It is incorporated in the SISM of Bertsch, Scholten and Esbensen [13,14] who model the nuclear surface as a semi-infinite slab of nuclear matter with a surface potential chosen similar to typical finite-nucleus optical potentials. The response function $S_{ST}(q,\omega)$ which is constructed from the SISM eigenstates and the probing field near the surface includes the effects of the residual interaction V_{ph} in an RPA framework. The residual interaction is strongly attractive in the T = 0, S = 0 channel and shifts the response function dramatically towards lower ω [13,14,16]. V_{ph} is weak in the T = 0, S = 1 channel and repulsive in both the T = 1, S = 0 and the T = 1, S = 1 channels. The corresponding shifts in the response function have a direct impact on the predicted cross sections $d^2\sigma/d\omega d\Omega$ (see equation 1). Whether a particular spin observable is modified by the residual interaction depends on how the related NN observable varies versus T_L^{eff} when separated into S=1 and S=0 channels. The effect of including 2p2h damping in the RPA response has been estimated by Smith and Wambach [15,16] using the formalism of Drożdż *et al* [30]. In all but the T=0, S=0 channel where there is no 2p2h effect, the response function is reduced at moderate ω and shifted towards high ω. For Gamow Teller excitations (T = 1, S = 1) 2p2h damping has been invoked by Bertsch and Hamamoto [31] to explain the quenching of L=0 strength in (p,n) reactions on heavy nuclei. The effect of

2p2h damping in the quasielastic regime should be more readily observable in the (p,n) or (n,p) cross sections or the spin-flip cross sections in (p,p′) rather than in the (p,p′) cross sections which have a large T=0, S=0 component.

In Figure 3 the spin observables are compared to the SISM results of Smith [16]. The dashed lines represent the free response without residual interaction, the solid curves include contributions from 2p2h damping and from two-step processes. The calculated observables $D_{ll'}$, $D_{ss'}$, $D_{ls'}$ and $D_{sl'}$ are predicted to be very close to the quasifree values showing little sensitivity to the residual interaction, and to inclusion of 2p2h damping or two-step processes. We observe that the data are shifted from the predictions over the entire ω range. Since such shifts are suggested by the RIA calculations at the quasielastic point one may ascribe them, at least partially, to a modification of the NN interaction at nuclear densities. It remains to be shown for quasielastic scattering whether there is a nonrelativistic equivalent of the enhancement of the lower Dirac components. For elastic scattering it was shown by Thies [32] that velocity-dependent nonrelativistic potentials can be constructed which produce observables that are indistinguishable from the relativistic predictions.

The SISM predicts D_{nn}, P and A_y values which are substantially different from the free values. For these observables the slopes versus ω are mainly caused by the residual interaction and are found to be in reasonable agreement with the data although the absolute values for P and A_y are considerably larger than the data. As was already discussed the latter discrepancy may be attributed to a fundamental density dependence of the NN interaction. The effects of 2p2h damping and of two-step processes on D_{nn} and on P or A_y are shown in Figure 4. In addition to the free response (short dashed lines) we show the cumulative effects of 1p1h RPA, of 2p2h damping, and of two-step contributions. The 1p1h RPA response is causing most of the deviation from the free response at small ω.

The calculations in Figures 3 and 4 assume the simple factorized form for cross section and spin observables (equation 1). Rather than performing at each ω and q the integral over the momenta $\vec{p}_2$ of the struck nucleon the NN observables are obtained at a representative

specific momentum $\vec{p}_2 = -\alpha\vec{q}$ which is assumed to be parallel to the only preferred direction $\vec{q}$. In the 'brickwall' or Breit frame $\vec{p}_2 = -\vec{q}/2 = -\vec{p}'_2$. This frame is most suitable for elastic scattering from the nucleus, i.e. for $\omega = 0$. For inelastic scattering it is more appropriate to evaluate the NN observables in the 'optimal' frame of Gurvitz [33]. The relativistic form of the optimal frame implies

$$\vec{p}_2 = -\vec{q}\left[\frac{1}{2} - \frac{\omega}{q}\sqrt{1 + \frac{4m^2}{q^2 - \omega^2}}\right] \tag{27}$$

In Figure 5 we show T_L^{eff} corresponding to both the Breit frame and the optimal frame for the range of ω values of the present experiment and for several scattering angles. At small scattering angles the 'optimal' momentum may exceed the Fermi momentum of the nucleus. We have omitted these unphysical values in Figure 5. It is expected [16] that this problem no longer arises if distortion effects are also taken into account. The optimal frame has the desirable property that it reduces to the Breit frame at $\omega = 0$ and that $T_L^{eff} = T_{lab}$ at the quasielastic point. The Breit frame is clearly unphysical for large momentum and energy transfers. In practice the Breit frame may still give acceptable numerical results provided the specific NN observable depends only weakly on T_L^{eff}.

In Figure 6 we show how the treatment of Fermi momentum averaging influences the quasifree observables. To avoid numerical inconsistencies in the evaluation of the NN observables in different codes we have used the RIA computer code throughout to obtain the results in Figure 6. It is seen that the optimal frame (dotted lines) provides a close approximation to explicit Fermi motion averaging (solid lines). Furthermore, the derivation of the optimal frame starting from the general projectile-nucleus scattering operator [33] provides justification for the use of on-shell NN amplitudes.

Use of the Breit frame (dashed lines) introduces slopes for $D_{ll'}$, $D_{ss'}$, $D_{ls'}$ and $D_{sl'}$ which are opposite in sign compared to the Fermi-averaged values and the experimental data. For P, A_y, and to a lesser extent D_{nn}, the Breit frame gives acceptable results. The deviations from the Fermi-averaged values are much smaller than the changes resulting from the SISM (see Figure 5).

V. SMALL-ANGLE (p,p') AND (n,p) RESULTS AND THE SISM

In the following section we discuss in terms of the SISM cross sections, analyzing powers and spin-flip probabilities measured between 3.1° and 15° for (p,p') at 290 MeV and cross sections between 0° and 12° for ^{54}Fe(n,p) obtained by Vetterli *et al.* [17] at 298 MeV. Comparisons with the RIA will not be shown since it does not include effects of the residual interaction which strongly modify A_y and S_{nn}. The SISM results were obtained by evaluating the NN amplitudes in the Breit frame. This is justifiable only for A_y and S_{nn} since the T_L^{eff} values associated with small energy and momentum transfers in the Breit frame adequately simulate Fermi momentum averaging (see Figure 6). The main reason for using the Breit frame over the optimal frame is the greater reliability in predicting strength and spin-flip strength distributions.

The spin observables A_y and S_{nn} are shown in Figures 7 and 8, respectively. In these and the following figures the free response is represented by short-dashed lines. The SISM RPA response including 2p2h damping and two-step contributions is represented by the solid lines. Although the slope of A_y versus ω is well reproduced by the SISM the calculations are above the data at nearly the complete range of momentum and energy transfers. As was already discussed in the previous section this is a strong indication that the NN interaction at nuclear densities differs from the free NN interaction, an effect which is implied by the RIA.

The qualitative features of the spin-flip probability S_{nn}, i.e. the decrease from the free NN values towards small ω and the rise towards large ω, is well reproduced by the SISM . This can be understood if one distinguishes the cross sections σ^{TS} and spin-flip probabilities S_{nn}^{TS} according to isospin and spin transfer $\{T,S\}$. Since $S_{nn}^{T0} \approx 0$ we may write

$$S_{nn} \approx \frac{\sum_T \sigma^{T1} S_{nn}^{T1}}{\sum_{TS} \sigma^{TS}} \tag{28}$$

Because of the strongly attractive residual interaction in the T=0, S=0 channel, σ^{00} dominates at small ω and forces S_{nn} to vanish. This, and the repulsive residual interaction V_{ph} in the S = 1 channels causes the rise of S_{nn} at large ω. At the highest ω, for intermediate

angles, S_{nn} is significantly enhanced relative to the free values, and this strong enhancement is not predicted by the SISM . The enhancement of S_{nn} has first been discussed by Glashausser *et al* [35]; it was shown that it corresponds to a nuclear response which is more than 80% S = 1 in this region. It has been observed at similar values of q and ω in a variety of (p,p') experiments on ^{12}C at 319 MeV [34], ^{24}Mg at 250 MeV [22], ^{40}Ca at 318 [35] and 800 MeV [34], ^{44}Ca at 290 MeV [34], and ^{90}Zr at 319 MeV [36]. The persistence of the enhancement at similar q for different target nuclei and to values of ω as large as 75 MeV [34] seems to rule out that it can be associated with a particular multipolarity.

One may speculate that the enhancement of S_{nn} is either the result of depletion of the S = 0 strength ($\sigma^{00} + \sigma^{10}$) or of an enhancement of the S = 1 strength ($\sigma^{01} + \sigma^{11}$). In principle this can be decided from a comparison of predicted and measured spin-flip strengths

$$\sigma S_{nn} \approx \sum_T \sigma^{T1} S_{nn}^{T1} \tag{29}$$

which do not involve the S=0 channels. In Figures 9 and 10 we show the cross sections and spin-flip cross sections together with the free response (dashed lines) and the predictions of the surface RPA (solid lines).

In Figure 11 we show explicitly for one angle (10°) the effects of 2p2h damping and of two-step contributions on cross sections (top) and spin-flip cross sections (bottom). In Figure 11 predictions for the free response (short-dashed) and for two-step contributions (long-dashed lines) are shown separately. The cumulative effects of the 1p1h RPA and two-step contributions (long-dashed curves), and of 2p2h damping (solid curves) are also shown. Inclusion of the 1p1h RPA correlations causes substantial shifts for both σ and σS_{nn}. The 2p2h damping and the two-step contributions are more significant for σS_{nn}. At large ω values the predicted values of σS_{nn} (Figure 10) are too small for all angles except for 15°. The predicted cross section σ (Figure 9) is underestimated at small angles and somewhat overestimated at large angles and high ω. At small momentum transfers for $\omega < 20$ MeV the nuclear response exhibits giant resonances of low multipolarity which depend sensitively on nuclear size and shell structure. In these regions the SISM response

is no longer a good approximation. The cross sections are also more sensitive than S_{nn} to details of the calculation such as two-step processes, distortions, and Fermi-momentum averaging. The agreement between theoretical and experimental S = 0 and S = 1 strengths at high ω is probably as good as can be expected, but it is difficult to determine whether the S_{nn} enhancement is due to an enhancement of the S=1 spin response, or a depletion of the S = 0 response. Microscopic RPA calculations for ^{40}Ca [37] suggest it is a combination of the two.

The cross sections for the ^{54}Fe(n, p)^{54}Mn reaction at 298 MeV [17] are compared to the surface RPA calculations in Figure 12. The (n,p) reaction involves only the T=1 channel and is predominantly S = 1. The dominance of a single $\{T, S\}$ channel is the likely reason for the good agreement of theory with experiment at laboratory angles of $5° - 12°$. The role of 2p2h damping which moves T = 1, S = 1 strength from regions of lower to higher ω is shown for the 8° data in Figure 13. This mechanism which has been invoked by Bertsch and Hamamoto to explain the quenching of the low-lying Gamow Teller strength [31] was originally thought to require a very strong tensor force but is now compatible with the weaker tensor force of the Bonn potential [30]. Compared to the (n,p) results the SISM is less successful in explaining cross sections and spin-flip cross sections in (p,p′) (see Figures 9-11). The SISM is also less successful in describing the ^{54}Fe(p,n)^{54}Co data at 300 MeV (see Fig. 12 in ref. 17).

VI. ISOSPIN, SPIN AND ANGULAR MOMENTUM COMPONENTS OF THE (p,p′) RESPONSE

We now discuss the extraction of giant resonance information from the small-angle (p,p′) data. We assume that angular distribution shapes for cross sections σ and spin-flip probabilities S_{nn} can be calculated with reasonable accuracy using the DWIA code DW81 [38] and the Franey-Love effective interaction [39] which does not include density dependence. Transition densities for populating giant resonances are typically described by the shell model or the finite-nucleus RPA and are outside the scope of the SISM. In the conventional analysis of (p,p′) cross sections [40,41,42] the resonances are superimposed

on a smooth 'background' which is assumed to be either a Gaussian plus exponential tail or have the same shape as calculated by the surface RPA. We follow here a more justifiable approach in which we use cross sections for (n,p) and (p,p′) to distinguish the nuclear response according to the isospin of the final states, and the additional information on spin-flip strength in (p,p′) to separate the spin transfer channels S = 0 and S = 1. Multipole strengths can then be extracted separately for S = 0 and S = 1 resonances. Similar analyses have recently been presented by Baker *et al* [43]. It is expected that this separation produces giant resonance strengths with smaller systematic errors since our procedure is based on a larger data set and is self-consistent.

The $T_f = 1, 2$ components of the (p,p′) response

The (n,p) reaction on the $T = 1$, $T_z = 1$ nucleus ^{54}Fe is the most selective of the (N,N) reactions since it only populates the $T = 2$, $T_z = 2$ levels in the residual nucleus ^{54}Mn. The target nucleus is fully polarized in isospin space, the isopin coupling coefficient being unity. The isovector strength in (p,p′) is split between the $T_f = 1$ and $T_f = 2$ states. Assuming nuclear interactions to be isospin symmetric the $T_f = 2$ (p,p′) strength can be calculated simply from the (n,p) cross section at the same angle. The isospin Clebsch-Gordan coefficients for the (p,p′) reaction differ from those for (n,p) by factors of $1/\sqrt{2}$ for both target and projectile, implying a reduction in strength by a factor of 1/4. The (n,p) cross sections have to be shifted to negative Q-values by the Coulomb shift of 8.60 MeV. The more negative reaction Q-value implies a further reduction of the (p,p′) cross section by a factor ($\approx$ 0.9 for L=0) which was estimated by DWIA calculations. In Figure 14 we show the (p,p′) cross sections together with histogram columns representing the $T_f = 2$ components. Since the (n,p) data [17] are not available outside of $\theta_{lab} = 12°$ the $T_f = 2$ components could not be obtained for the 15° data. Because the (p,p′) cross sections have a very strong S=0 isoscalar component the $T_f = 2$ component is quite small at all momentum and energy transfers.

For the isospin decomposition of the spin-flip strength σS_{nn} we require the spin-flip probability for the (n,p) reaction, $S_{nn}^{T=1}$. Although this quantity has not been measured it

can be calculated quite reliably. The (n,p) reaction is purely isovector and at these energies 90% dominated by S = 1 as can be seen from the NN amplitudes [20]. Furthermore, the residual interaction is repulsive in both the T=1, S=0 and T=1, S=1 channels and therefore should cause no ω dependence of $S_{nn}^{T=1}$. This is confirmed by S_{nn} measurements for (p,n) reactions at 0° [44,45] which show values close to the free NN values over most of the ω range (the exceptions are discrete states such as the isobaric analog state which cannot be populated in (n,p) reactions). The $T_f = 2$ part of the spin-flip strength was calculated separately for L=0 and higher multipoles. The multipole decomposition of the (n,p) cross sections [17] was used and $S_{nn}^{T=1}$ was obtained either from the SISM (for L≥1, see Table III) or from DWIA calculations (for L=0). The resulting spin-flip strength in (p,p') is shown in Figure 15 together with histogram columns representing the $T_f = 2$ components. Because of the absence of the strong isoscalar S=0 channel the $T_f = 2$ component is now a substantial fraction of the total spin-flip strength.

Multipole decomposition of S=1 strength

The decomposition of the spin-flip strength distributions of Figure 15 into angular momentum transfers L makes use of the well-known fact that cross section maxima for larger L values occur at larger momentum transfers. Theoretical angular distributions were generated for each multipole using the DWIA. To estimate the systematic uncertainties in the extraction of the multipole components we have used transition densities for two different shell model configurations. For decomposition (A) we have calculated the L=0 part as the sum of all 1^+ states connected to a pure $\pi[f_{7/2}]^6\nu[f_{7/2}]^8$ ground state. This model corresponds to the Tamm-Dancoff approximation (TDA) without RPA correlations. With the shell model code OXBASH [46] and the residual interaction of van Hees [47] we obtain six $T_f = 2$ states between E_x = 8.3 and 12.9 MeV, and 18 $T_f = 1$ states between E_x = 3.96 and 11.57 MeV. For the latter states we have ignored the interference from the isoscalar part of the NN interaction which is poorly known [22] at nuclear densities and which may introduce an uncertainty of perhaps ±20% in the calculated cross sections. For the higher multipolarities we have assumed simple final states: L = 1 : $[f_{7/2}^{-1}, g_{9/2}]_{1^-}$; L = 2 : $[f_{7/2}^{-1}, f_{5/2}]_{3^+}$. The nonrelativistic optical potential of Table II was used to compute angular distributions of σS_{nn} for E_x = 0−50 MeV in 10 MeV intervals. Interpolated shapes for 1 MeV wide energy bins were used to fit [17,48] the experimental angular distributions. Typical results are shown in Figure 16. In Figure 17 we show the spin-flip strength at 3.1° together with the L=0 component (hatched area, lower panel) and at 5.0° with the L=1 component (upper panel). The spin dipole response is similar in shape to that observed in ^{40}Ca [43]. The L=0 components above ω = 14.5 MeV are not shown since they are only a small fraction of the total σS_{nn} and vary widely from bin to bin. At θ_{cm} = 3.18° the sum of the L=0 spin-flip strength between 4.5 and 14.5 MeV is $(d\sigma/d\Omega)_{CM}$ = 2.6 ± 0.3 mb/sr where the error includes uncertainties from counting statistics and from the decomposition. The centroid of the L=0 strength distribution is at ∼ 10.3 MeV which is comparable to the 201 MeV (p,p') data of Djalali *et al* [49] (S=1, L=0 centroid at 10.04 MeV) and the (e,e') data of Eulenberg *et al* [50] (B(M1) centroid at 10.5 MeV) but substantially higher than 8.6 MeV, the TDA prediction. The difference arises from the absence of significant $T_f = 1$, 1^+ strength below 8 MeV in the experimental spectra.

In a second decomposition (B) coherent states of a particular L,J were constructed [51] by applying an operator $r^L[Y_L \times \sigma]_J$ to the simple $f_{7/2}^{14}$ ground state. From these states a single $L = 1$ angular distribution was obtained from the sum of $0^-, 1^-$ and 2^- coherent states, and similarly for L=2 and L=3. The L=0 angular distribution arises in this model from a single $f_{7/2}^{-1}f_{5/2}$ transition amplitude. The θ_{cm} = 3.18° L=0 component between 4.5 and 14.5 MeV amounts to spin-flip strength of $(d\sigma/d\Omega)_{CM}$ = 2.4 ± 0.3 mb/sr independent of whether L=3 components are included in the decomposition or not. The L=1 strength is spread out over tens of MeV and varies substantially depending on whether L > 2 multipoles are included or not.

The average of the L=0 strength from decompositions (A) and (B), at θ_{cm} = 3.18° and between 4.5 and 14.5 MeV excitation, is $(d\sigma/d\Omega)_{CM}$ = 2.5 ± 0.3 mb/sr. From the (n,p) results of Vetterli *et al* [17] we estimate that the $T_f = 2$, L=0 differential cross section in this energy interval is (1.9 ± 0.1) mb/sr. This estimate takes the Coulomb shift of 8.6

MeV, the isospin factors of 0.25, and DWIA extrapolations to $\theta_{cm} = 3.18°$ into account. The spin-flip probability is calculated to be $S_{nn} = 0.53$ for the the $T_f = 2$ states. Thus we find that the T_f=2 states receive (1.0 ± 0.1) mb/sr of the experimental spin-flip strength. The remaining (1.5 ± 0.3) mb/sr are attributed to the $T_f = 1$ states.

For comparisons with theory of L=0 strengths in the (n,p), (p,p′) and (p,n) reactions it is desirable to sum the strength over similarly large energy intervals. Because of poorer statistical accuracy and a larger contribution of spin dipole states at $\theta_{cm} = 3.18°$ the useful range of the (p,p′) decomposition is smaller (upper limit 14.5 MeV) than that of the (n,p) reaction (upper limit 10 MeV in ^{54}Mn, corresponding to 18.6 MeV in ^{54}Fe). We have estimated the likely additional strength located between 14.5 and 18.6 MeV from the (n,p) reaction where about 12% of the total L=0 strength from 0-10 MeV is in the 4 MeV interval between 6 and 10 MeV excitation [17]. A similar fraction is located in a 4 MeV interval above the bulk of the ^{54}Fe(p,n) strength in ^{54}Co [17]. For theoretical comparisons we have added (10 ± 10%) to the spin flip strength between 4.5 and 14.5 MeV. The estimated total spin flip strength below 18.6 MeV, (2.75 ± 0.4) mb/sr, can be compared to nuclear structure calculations if $\hat{\sigma}$, the cross section per unit of B(GT), is known. We adopt here the value $\hat{\sigma}$(q=0,ω=0)=5.1 ± 0.8 mb/sr which was determined at 300 MeV by Vetterli *et al* [17] from the ^{54}Fe(p,n) transition to the 0.94 MeV state in ^{54}Co. The B(GT) value for this transition, (0.73 ± 0.10), had been determined previously by (p,n) reactions at 135 and 160 MeV [52,53] using typical $\hat{\sigma}$ values for this mass region. We note that this experimentally determined value of $\hat{\sigma}$ is consistent with empirical systematics for nuclei with A=6-54 and energies between 135-492 MeV [54]. The $\hat{\sigma}$ value is however much larger than the value of 3.6 mb/sr which is obtained with the DWIA using the Franey-Love interaction [39] and the optical potential of section 2. The reason for this failure of the DWIA which should affect the L=0 cross sections for the (p,n), (p,p′) and (n,p) reactions by similar renormalization factors is not known.

With the simple TDA model and $\hat{\sigma} = 5.1$ mb/sr we calculate large values of 9.7, 3.3 and 6.4 mb/sr for total, $T_f = 2$, and $T_f = 1$ spin-flip strengths, respectively. The quenching

factor $\sigma_{exp}/\sigma_{theory} \sim 0.3$ can be attributed to the restricted model space for the valence nucleons in the TDA. The effects of an expanded shell model space have been studied by Bloom and Fuller [55] and by Muto [56]. Even larger reductions of the theoretical strengths are obtained by Auerbach, Zamick and Klein [57] when RPA correlations are included. In Table IV we compare L=0 strength obtained at TRIUMF near 300 MeV for ^{54}Fe(n,p), (p,p′) and (p,n) reactions with theoretical predictions. It should be noted that all theoretical cross sections have a large, but common, systematic uncertainty which arises from the conversion of the matrix elements of the one-body operators $\sigma\tau_-$, $\sigma\tau_0$ and $\sigma\tau_+$ to cross sections. We have assumed that the reduction factors for the L=0 strength implied in going from the TDA to the RPA are the same in ^{60}Ni [57] and in ^{54}Fe. The results of the quasi-particle RPA of Engel, Vogel and Zirnbauer [58] were only available for the charge exchange reactions and have been scaled for the (p,p′) channel.

The quenching factors, $\sigma_{exp}/\sigma_{theory}$, determined at incident energies of 290-300 MeV for the three reactions are shown in Figure 18. Since the relative comparison of the reactions is of primary interest the errors include contributions from counting statistics and multipole decomposition but not the systematic uncertainties in $\hat{\sigma}$ which are common to the three reactions. The theoretical calculations (TDA, RPA and QRPA) do not include extra-nucleonic degrees of freedom such as Δ-hole excitations and thus satisfy the sum rule for β^- and β^+ GT strength, $\sum$B(GT$^-$) - $\sum$B(GT$^+$) = 3 (N - Z). The reduction of L=0 strength from the simple TDA estimates is predicted to be most severe in the (n,p) direction, intermediate for (p,p′), and least severe for (p,n). The experimental data in Table IV confirm this. The QRPA calculations [58] predict the smallest GT strength and quenching factors which agree within errors for both (p,n) and (n,p) reactions. The quenching factors for (p,p′) are lower than those for the (p,n) and (n,p) reactions. Several reasons might be responsible for this. First we rely on S_{nn} values calculated in the DWIA which might be larger than the actual ones. Since isospin symmetry can be invoked for the $T_f = 2$ states the small spin-flip strength might be attributed to the $T_f = 1$ states for which we have neglected the interference of the isoscalar with the dominant isovector

amplitudes.

The QRPA quenching factors of ≈0.65 are comparable to those for the low-energy excitation region in (sd) shell nuclei [21,22,59] where untruncated (sd) shell model calculations are available. The structure calculations agree with experiment if an effective axial-vector coupling constant $(g_A/g_V)_{eff} \approx 1$ is used. The cause of the quenching of GT strength may be attributed to 2p2h damping [30,31] (for which we have provided some evidence in section IV) and/or to coherent Δ-hole excitations [60].

Multipole decomposition of S=0 strength

The determination of the S=0 strength requires subtraction of the S = 1 component from the (p,p′) cross section σ. This subtraction is model dependent since S_{nn} differs from unity for pure S = 1 transitions. We define a quantity $S_{nn}^{S=1}$ (α in [43])

$$S_{nn}^{S=1} = \frac{\sigma^{01} S_{nn}^{01} + \sigma^{11} S_{nn}^{11}}{\sigma^{01} + \sigma^{11}}$$

which can be calculated in the surface RPA model. The values for $S_{nn}^{S=1}$ shown in Table V are very similar to those for $S_{nn}^{T=1}$ (see Table III) since both are dominated by the spin-flip isovector NN amplitudes. The S=0 cross sections

$$\sigma_{S=0} = \sigma_{exp} - \frac{(\sigma S_{nn})_{exp}}{S_{nn}^{S=1}}$$

are shown in Figure 19 for the five angles of the experiment.

We have carried out a multipole decomposition of $\sigma_{S=0}$ similar to the one described previously for σS_{nn}. The angular distributions for the multipoles L=1-4 were generated using the coupled channels program ECIS79 [61] which includes Coulomb excitation and relativistic kinematics. We did not include a giant monopole resonance because it is found to be anomalously weak in ^{40}Ca and ^{58}Ni [41]. A first order vibrational model was used in the collective DWBA calculations as described elsewhere [42]. The transition potential arises from the distortion of the five separate terms of the optical potential (real, imaginary, real spin-orbit, imaginary spin-orbit, and Coulomb). The magnitude of the cross sections is proportional to the square of deformation lengths ($\beta_L R$), where the $R = r_x A^{1/3}$

are appropriately chosen radii for each of the five potentials. For giant resonances it is customary [40] to express the deformation lengths in terms of the energy weighted sum rule (EWSR) strengths as

$$(\beta_1 R) = \frac{8\pi\hbar^2}{m}\frac{NZ}{AE_x} \qquad L = 1$$

$$(\beta_L R) = \frac{2\pi\hbar^2}{3m}\frac{L(L+1)}{A^3 E_x} \qquad L \geq 2$$

The angular distributions for each multipole are calculated assuming that 100% of the EWSR is concentrated at each energy bin. A least-squares fit of the $\sigma_{S=0}$ data give directly the fraction of the EWSR for each multipole and energy. By carrying out multipole decompositions with various different multipole combinations (L=1,2,3,4) we have estimated the systematic error associated with the decomposition. Higher multipoles (L≥3) are unreliable because of the limited angular range of the data.

The results from one of these decompositions (L=1-4 included) are shown in Fig. 20. The isovector giant dipole resonance (IVGDR) is found to peak near 19.5 MeV but persists to higher excitation in agreement with previous photoabsorption data for ^{54}Fe [62]. The summed dipole strength between 13-25 MeV is (88 ± 7)% EWSR, and between 13-30 MeV is (123±12)% EWSR. The dipole strength is qualitatively similar to that found in this mass region by photon absorption experiments [63].

The quadrupole strength has a maximum near 16 MeV in agreement with previous (p,p′) data for ^{58}Ni [41]. The isoscalar character of this resonance can be inferred from a comparison with other probes, e.g. (α, α') [64]. The quadrupole strength strongly depends on whether L=3, or L=4, or both, are included in the decomposition. For the 11-22 MeV region the summed quadrupole strength is estimated to be (55±13)% EWSR. A similar amount of quadrupole strength, (50±10)%, has been found in ^{58}Ni(p,p′) [41]. The quadrupole strength above 23 MeV depends on the decomposition and is compatible with zero.

We emphasize that in contrast to some previous (p,p′) giant resonance analyses [41,42] no adhoc separation of the cross section into resonance and background contributions had

to be made. The agreement between both types of analyses demonstrates that the smooth background fitted in previous (p,p') analyses is mainly of S = 1 character.

VII. CONCLUSIONS

The comprehensive data set for the ^{54}Fe(p,p') reaction from this work has been confronted with current models of inclusive nucleon scattering from nuclei. A complete set of spin observables at 20° disagrees in detail with all the models. The surface RPA model of Bertsch, Scholten and Esbensen describes well the slope versus ω observed for A_y and S_{nn}. We have shown that Fermi momentum averaging should either be included explicitly, or the 'optimal frame' rather than the Breit frame should be employed for the NN kinematics to simulate Fermi motion.

The nonrelativistic models are unable to predict the systematic lowering of A_y observed at all momentum and energy transfers. This feature is reproduced in the relativistic model of Horowitz, Murdock and Iqbal by using an effective mass parametrization which is associated with an attractive scalar potential acting on nucleons at high densities. The inclusion of the RPA correlations into the relativistic model is still to be accomplished. Therefore this model is reliable numerically, for A_y and S_{nn}, under quasielastic kinematic conditions only.

The SISM is qualitatively most successful in predicting the spin-flip probability. However, the enhancement of S_{nn} above the SISM predictions, at momentum transfers of $q \sim 100$ MeV/c and $\omega > 20$ MeV, is not reproduced, although the enhancement is a general feature observed in many nuclei [34]. Continuum RPA calculations suggest [34] that the enhancement is the result of the combined effects of a strong concentration of S = 0 strength at lower energy, and a shift of S = 1 strength to higher energy.

The availability of comprehensive data for (p,p') and (n,p) has allowed us to separate both cross section and spin-flip strength with respect to isospin of the final states, $T_f = 1, 2$. Since the spin-flip strength is purely S = 1, the non spin-flip strength $\sigma_{S=0}$ could be obtained by subtracting from the cross sections the S = 1 part. These separations are model dependent since spin-flip probabilities $S_{nn}^{T=1}$ and $S_{nn}^{S=1}$ are required which have not

been measured. We believe however that the model dependence is slight because both quantities are dominated by the T = 1, S = 1 channel which can be reliably calculated by the surface RPA. We have performed a multipole analysis both of σS_{nn} and of $\sigma_{S=0}$. The quenching of S=1, L=0 strength is slightly more severe than that found for (n,p) and (p,n) reactions on ^{54}Fe. For the latter reactions the Gamow Teller quenching factors are compatible with QRPA calculations using an effective coupling constant $g_A/g_V \sim 1$. The strengths extracted from $\sigma_{S=0}$ for the giant dipole and quadrupole resonances are compatible with conventional giant resonance analyses based on σ. This indicates that the smooth background underlying these resonances is mainly of S = 1 character.

The authors would like to thank B.A. Brown, H. Esbensen, C. Horowitz and D. Murdock for correspondence and comments on theoretical aspects of this work. This work was supported in part by grants from the Natural Sciences and Engineering Research Council of Canada and by the National Science Foundation and the US Department of Energy.

References

[1] P. Barreau, M. Bernheim, J. Duclos, J.M. Finn, Z.Meziani, J. Morgenstern, J. Mougey, D. Royer, B. Saghai, D. Tarnowski, S. Turck-Chieze, M. Brussel, G.P. Capitani, E. de Sanctis, S. Frullani, F. Garibaldi, D.B. Isabelle, E. Jans, I. Sick, and P.D. Zimmerman, Nucl. Phys. A402, 515 (1983).

[2] Z.E. Meziani, P. Barreau, M. Bernheim, J. Morgenstern, S. Turck-Chieze, R. Altemus, J. McCarthy, L.J. Orphanos, R.R. Whitney, G.P. Capitani, E. de Sanctis, S. Frullani, and F. Garibaldi, Phys. Rev. Lett. 52, 2130 (1984); 54, 1233 (1984).

[3] M. Deady, C.F. Williamson, P.D. Zimmerman, R. Altemus, and R.R. Whitney, Phys. Rev. C33, 1897 (1986).

[4] R.D. Smith and S.J. Wallace, Phys. Rev. C32, 1654 (1987).

[5] B.C. Clark, S. Hama, R.L. Mercer, L. Ray and B. Serot, Phys. Rev. Lett. 50, 1644 (1983); and J.A. McNeil, J.R. Shepard and S.J. Wallace, Phys. Rev. Lett. 50, 1439 (1983).

[6] D.P. Murdock and C.J. Horowitz, Phys. Rev. C35, 1442 (1987).

[7] C.J. Horowitz and J. Iqbal, Phys. Rev. C33, 2059 (1986).

[8] C.J. Horowitz and D.P. Murdock, Phys. Rev. C37, 2032 (1988).

[9] O. Häusser, Can. J. Phys. 65, 691 (1986).

[10] X.Y. Chen, L.W. Swenson, F.Farzanpay, D.K. McDaniels, Z. Tang, Z. Xu, D. . Drake, I. Bergqvist, A. Brockstedt, F.E. Bertrand, D.J. Horen, J. Lisantti, K. Hicks, M. Vetterli, and M.J. Iqbal, Phys. Lett. B205, 436 (1988).

[11] T.A. Carey, K.W. Jones, J.B. McClelland, J.M. Moss, L.B. Rees, N. Tanaka, and A.D. Bacher, Phys. Rev. Lett. 53, 144 (1984).

[12] O. Häusser, R. Abegg, R.G. Jeppesen, R. Sawafta, A. Celler, A. Green, R.L. Helmer, R. Henderson, K. Hicks, K.P. Jackson, J. Mildenberger, C.A. Miller, M.C. Vetterli, S. Yen, M.J. Iqbal, and R.D. Smith, Phys. Rev. Lett. 61, 822 (1988).

[13] G. Bertsch and O. Scholten, Phys. Rev. C25, 804 (1982); H. Esbensen and G. Bertsch, Ann. Phys. 157, 255 (1984).

[14] H. Esbensen and G. Bertsch, Phys. Rev. C34, 1419 (1986).

[15] R.D. Smith and J. Wambach, Phys. Rev. C38, 100 (1988).

[16] R.D. Smith, in Proceedings of International Conference on Spin Observables of Nuclear Probes, Telluride, Colorado, March 13-17, 1988, ed. by C.J. Horowitz, C.D.Goodman, and G.E. Walker, (Plenum, New York, 1988)p.15.

[17] M.C. Vetterli, O. Häusser, R. Abegg, W.P Alford, A. Celler, D. Frekers, R. Helmer, R. Henderson, K. Hicks, K.P. Jackson, R.G. Jeppesen, C.A. Miller, K. Raywood, and S. Yen, Phys. Rev. C40, 559 (1989); M.C. Vetterli *et al*, Phys. Rev. Lett. 59, 439 (1987).

[18] R. Abegg, G.S. Clark, M.K. Craddock, W. Felske, T. Gathright, A. Otter, P. Reeve, R. Schubank, G.M. Stinson, and S. Yen, Nucl. Inst. Meth. A273, 43 (1988).

[19] R. Abegg and R. Schubank, TRIUMF design note TRI-DN-87-17 (1987).

[20] R.A. Arndt and L.D. Roper, Scattering Analysis Interactive Dial-in (SAID) program, unpublished.

[21] O. Häusser, R. Sawafta, R.G. Jeppesen, R. Abegg, W.P. Alford, R.L. Helmer, R. Henderson, K. Hicks, K.P. Jackson, J. Lisantti, C.A. Miller, M.C. Vetterli, and S. Yen, Phys. Rev. C37, 1119 (1988).

[22] R.S. Sawafta, O. Häusser, R. Abegg, W.P. Alford, R. Henderson, K. Hicks, K.P. Jackson, J. Lisantti, C.A. Miller, M.C. Vetterli, and S. Yen, Phys. Lett. B201, 219 (1988).

[23] R.S. Henderson, O. Häusser, K. Hicks, C. Günther, W. Faszer, R. Sawafta, and N. Poppe, Nucl. Instrum. Methods A254, 61 (1987).

[24] O. Häusser, R.S. Henderson, K. Hicks, D.A. Hutcheon, D. Clark, C. Günther, R. Sawafta, and G.W. Waters, Nucl. Instrum. Methods A254, 67 (1987).

[25] J.B. McClelland, J.F. Amann, W.D. Cornelius, H.A. Thiessen, and B. Aas, LAMPF preprint LA-UR-84-1671.

[26] Ma Ji, M. Sc. thesis, Simon Fraser University, 1987.

[27] E. Aprile-Giboni et al., Nucl. Instrum. Methods 215, 147 (1983).

[28] G.G. Ohlsen, Rep. Prog. Phys. 35, 717 (1972); and references therein.

[29] B.D. Serot and J.D. Walecka, In *Advances in Nuclear Physics*, ed. by J.W. Negele and E. Vogt, (Plenum Press, New York, 1986) Vol. 16, p.116.

[30] S. Drożdż, V. Klemt, J. Speth and J. Wambach, Phys. Lett. B166, 18 (1986).

[31] G.F. Bertsch and I. Hamamoto, Phys. Rev. C26, 1323 (1982).

[32] M. Thies, Phys. Lett. B162, 255 (1985); B166, 23 (1986).

[33] S.A. Gurvitz, Phys. Rev.C33, 422 (1986).

[34] F.T. Baker, L. Bimbot, B. Castel, R.W. Fergerson, C. Glashausser, A. Green, O. Häusser, K. Hicks, K. Jones, C.A. Miller, S.K. Nanda, R.D. Smith, M. Vetterli, J. Wambach, R. Abegg, D. Beatty, V. Cupps, C. Djalali, R. Henderson, K.P. Jackson, R. Jeppesen, J. Lisantti, M. Morlet, R. Sawafta, W. Unkelbach, A. Willis, and S. Yen, Phys. Lett. B237, 337 (1990).

[35] C. Glashausser, K. Jones, F.T. Baker, L. Bimbot, H. Esbensen, R.W. Fergerson, A. Green, S. Nanda, and R.D. Smith, Phys. Rev. Lett. 58, 2404 (1987)

[36] S.K. Nanda, C. Glashausser, K.W. Jones, J.A. McGill, T.A. Carey, J.B. McClelland, J.M. Moss, S.J. Seestrom-Morris, H. Ohnuma, M. Franey, M. Gazzaly, and N. Hintz, Phys. Rev. Lett. 51, 1526 (1983).

[37] P.M. Boucher, B. Castel, Y. Okuhara, I.P. Johnstone, J. Wambach, and T. Suzuki, Phys. Rev. Rap. Comm. C37, 906 (1988).

[38] Program DWBA70, R. Schaeffer and J. Raynal (unpublished); extended version DW81 by J.R. Comfort (unpublished).

[39] M.A. Franey and W.G. Love, Phys. Rev. C31, 488 (1985).

[40] G.R. Satchler, Nucl. Phys. A224, 596 (1985).

[41] F.E. Bertrand, G.R. Satchler, D.J. Horen, and A. van der Woude, Phys. Lett. B80, 198 (1979).

[42] L.W. Swenson, X.Y. Chen, J. Lisantti, D.K. McDaniels, I. Bergqvist, F.E. Bertrand, D.J. Horen, E.E. Gross, C. Glover, R.O. Sayer, B.L. Burks, O. Häusser, K. Hicks, and J. Iqbal, Phys. Rev. C40, 246 (1989); and references therein.

[43] F.T. Baker, L. Bimbot, R.W. Fergerson, C. Glashausser, A. Green, K. Jones, K. Nakayama, and S. Nanda, Phys. Rev. C37, 1350 (1988); F.T. Baker, L. Bimbot, R.W. Fergerson, C. Glashausser, A. Green, K. Jones, W.G. Love, and S. Nanda, Phys. Rev. C40, 1877 (1989).

[44] T.N. Taddeucci, Can. J. Phys. 65, 557 (1987).

[45] J.W. Watson, B.D. Anderson, and R. Madey, Can. J. Phys. 65, 566 (1987).

[46] A. Etchegoyen, W.D.M. Rae, B.A. Brown, MSU-NSCL Report No. 524 (1984) unpublished,"The Oxford-Buenos Aires Shell Model Code".

[47] A.G.M. van Hees and P.W.N. Glaudemans, Z. Phys. A303, 267 (1981).

[48] M.A. Moinester, Can. J. Phys. 65, 660 (1987).

[49] C. Djalali, N. Marty, A. Willis, J.C. Jourdain, N. Anantaraman, G.M. Crawley, A. Galonsky, and J. Duffy, Nucl. Phys. A410, 399 (1983).

[50] G. Eulenberg, D.I. Sober, W. Steffen, H.D. Gräf, G. Küchler, A. Richter, E. Spamer, B.C. Metsch, and W. Knüpfer, Phys. Lett. B116, 113 (1982).

[51] B.A. Brown, private communication.

[52] B.D. Anderson, C. Lebo, A.R. Baldwin, T. Chittrakarn, R. Madey, J.W. Watson, and C.C. Foster, Phys. Rev. C41, 1474 (1990).

[53] J. Rapaport, T. Taddeucci, T.P. Welch, C. Gaarde, J. Larsen, D.J. Horen, E. Sugarbaker, P. Koncz, C.C. Foster, C.D. Goodman, C.A. Goulding, and T. Masterson, Nucl. Phys. A310, 371 (1983).

[54] O. Häusser *et al*, to be published.

[55] S.D. Bloom and G.M. Fuller, Nucl. Phys. A440, 511 (1985).

[56] K. Muto, Nucl. Phys. A451, 481 (1986).

[57] N. Auerbach, L. Zamick, and A. Klein, Phys. Lett. B118, 256 (1982); N. Auerbach, Phys. Rev. C36, 2694 (1987).

[58] J. Engel, F. Vogel, and M.R. Zirnbauer, Phys. Rev. C37, 731 (1988); and J. Engel, private communication.

[59] R. Madey, B.S. Flanders, B.D. Anderson, A.R. Baldwin, C. Lebo, J.W. Watson, S.M. Austin, A. Galonsky, B.H. Wildenthal, and C.C. Foster, Phys. Rev. C35, 2011 (1987).

[60] G.E. Brown and M. Rho, Nucl. Phys. A372, 397 (1981).

[61] J. Raynal, private communication.

[62] B.S. Ratner, A.N. Sergiyevsky and S.S. Verbitsky, Nucl. Phys. A285, 71 (1977).

[63] B.L. Berman and S.C. Fultz, Rev. Mod. Phys. 47, 713 (1975).

[64] F.E. Bertrand, Ann. Rev. Nucl. Sci. 26, 457 (1976).

Table I.

Relativistic optical model parameters for ^{54}Fe(p, p) elastic scattering at 290 MeV

The relativistic form of the potential assumes a Dirac equation of the form

$$\left[-i\vec{\alpha}\cdot\vec{\nabla}+\beta(m+U_0(r))+(E-U_1(r))\right]\Psi(\vec{r})=0$$

The scalar potential $U_0(r)$ is

$$U_0(r)=V_0\left[1+exp\left(\frac{r-r_R^0A^{1/3}}{a_R^0}\right)\right]^{-1}+iW_0\left[1+exp\left(\frac{r-r_I^0A^{1/3}}{a_I^0}\right)\right]^{-1}$$

and a similar expression defines the vector potential $U_1(r)$. The fitted parameters are

type	V (MeV)	r_R (fm)	a_R (fm)	W (MeV)	r_I (fm)	a_I (fm)
scalar	-456.7	1.013	0.691	77.89	1.106	0.843
vector	334.4	1.014	0.665	-96.87	1.054	0.825

Table II.

Nonrelativistic Woods-Saxon optical model parameters

for ^{54}Fe(p, p) elastic scattering at 290 MeV

The nonrelativistic optical potential is of the form

$$V(r) = V_{coul} + V_R f_R(r) + iW_I f_I(r) - (V_{RSO} g_{RSO}(r) + iW_{ISO} g_{ISO}(r))\vec{L} \cdot \vec{s}$$

where

$$f_i(r) = \left[1 + exp(\frac{r - r_i A^{1/3}}{a_i})\right]^{-1}$$

$$g_i(r) = \frac{1}{r}\frac{d}{dr} f_i(r)$$

This potential was used in the Schrödinger equation using relativistic kinematics and with the reduced mass replaced by the reduced total energy in the c.m. frame.

type	V_R (MeV)	r_R (fm)	a_R (fm)	W_I (MeV)	r_I (fm)	a_I (fm)
central	-17.81	1.028	0.445	-22.03	1.147	0.629
spin-orbit	-2.41	1.009	0.558	+0.45	0.942	0.587

Table III.

$S_{nn}^{T=1}$ calculated in the surface RPA model

for ^{54}Fe(p,p') at 290 MeV.

θ_{cm}	E_x = 10 MeV	E_x = 30 MeV	E_x = 50 MeV
3°	.590	.538	.470
5°	.526	.489	.440
7°	.456	.436	.412
10°	.407	.402	.398
15°	.424	.423	.427

Table IV.

L=0 strength for (n,p), (p,p') and (p,n) reactions with ^{54}Fe near 300 MeV

reaction	E_{lab} (MeV)	θ_{cm} (deg.)	ω (MeV)	observed	E_x^{max} (MeV)	L=0 strength (mb/sr) [a] exp.[b]	TDA[c]	RPA[d]	QRPA[e]
^{54}Fe(n,p)^{54}Mn	298	0	0	σ	10.0	15.7±0.7	52.5	29.8	25.6
^{54}Fe(p,p')	290	3.18	10.3	σS_{nn}	18.6	2.75 ± 0.4	9.7	~6.5	~ 5.6
^{54}Fe(p,n)^{54}Co	300	0	11.0	σ	15.0	37.5 ± 1.2	81.9	62.1	55.3

[a] assumes $\hat{\sigma}(q = 0, \omega = 0) = 5.1$ mb/sr

[b] the (n,p) and (p,n) data are from ref. 17.

[c] simple shell model assuming $f_{7/2}^{14}$ configuration for the ^{54}Fe ground state.

[d] scaled from RPA calculations for ^{60}Ni, see ref. 57.

[e] from ref. 58.

Table V.

$S_{nn}^{S=1}$ calculated in the surface RPA model

for ^{54}Fe(p,p') at 290 MeV.

θ_{cm}	E_x = 10 MeV[a]	E_x = 30 MeV	E_x = 50 MeV
3°	.662	.592	.516
5°	.593	.537	.478
7°	.503	.470	.433
10°	.400	.397	.384
15°	.306	.324	.332

[a] for 24 TDA 1^+ states between 4-13 MeV microscopic DWIA calculations yield an average value $< S_{nn} >= 0.58$ at $\theta_{cm} = 3°$.

FIGURE CAPTIONS

Fig.1. Cross sections (top) and analyzing powers (bottom) for elastic scattering of 290 MeV protons from ^{54}Fe. The results of Dirac and Schrödinger fits to the data are shown as solid and dashed lines, respectively.

Fig.2. Complete spin observables for inclusive proton scattering from ^{54}Fe at 20°. The dashed lines correspond to the Fermi-gas response using free NN observables. The solid lines include the enhancement of the lower Dirac components for both target and incident proton.

Fig.3. The same data as shown in Fig. 2 are compared to predictions of the SISM. The dashed lines correspond to the free response, the solid lines include the nuclear RPA response and two-step contributions as described in the main text.

Fig.4. Spin observables P and A_y (top) and D_{nn} (bottom) at 20° are compared to predictions of the SISM . Theoretical curves are for the free response (short-dashed lines), and for the cumulative effects of the 1p1h RPA (long-dashed), of 2p2h damping (short-long dashed), and of two-step contributions (solid lines).

Fig.5. Effective laboratory energies for quasielastic scattering at various scattering angle and ω values evaluated in the optimal (solid lines) or Breit frame (dashed lines).

Fig.6. The effect of Fermi-momentum averaging on the spin observables of Figs. 2 and 3 assuming the free NN response. The results were obtained by explicitly summing over the momenta of a Fermi gas (solid lines), or by assuming optimal frame kinematics (short-dashed lines), or Breit frame kinematics (long-dashed lines).

Fig.7. Analyzing powers compared to SISM predictions. The dashed lines correspond to the free response, the solid lines include the nuclear RPA response and two-step contributions as described in the main text.

Fig.8. Spin-flip probabilities compared to SISM predictions. The curves are explained in the caption of Fig.7.

Fig.9. Cross sections compared to SISM predictions. The curves are labelled as in Fig. 7. The two-step contribution are shown as long-dashed lines.

Fig.10. Spin-flip cross sections compared to SISM predictions. The curves are labelled as in Fig. 9.

Fig.11. Cross sections (top) and spin-flip cross sections (bottom) at 10° are compared to predictions of the SISM. The free response (short-dashed lines) and two-step contributions (long-dashed lines) are shown separately. The cumulative effects of the 1p1h RPA and of two-step contributions (short-long dashed lines), and of the further effect of 2p2h damping (solid lines) are also shown.

Fig.12. Cross sections for the ^{54}Fe(n,p) reaction compared to predictions of the SISM. The curves are labelled as in Fig. 9.

Fig.13. The ^{54}Fe(n,p) cross section at 8°. Theoretical curves are labelled as in Fig. 11.

Fig.14. Cross sections for inelastic proton scattering from ^{54}Fe at 290 MeV. The histogram columns show the population of $T_f = 2$ final states deduced from the (n,p) reaction. No (n,p) data were available for angles larger than 12°.

Fig.15. Spin-flip cross sections for inelastic proton scattering from ^{54}Fe at 290 MeV. The histogram columns are explained in the caption of Fig. 14.

Fig.16. Multipole decomposition of the (p,p′) spin-flip cross sections at three different values of ω. The curves represent the L=0 (short dashed), L=1 (long dashed), L=3 (short-long dashed), and total (solid lines) angular distributions.

Fig.17. Spin-flip cross sections at 5.0° and 3.1°. The cross-hatched areas show the L=1 (top) and L=0 (bottom) contributions. The L=0 fraction at $\omega > 15$ MeV is not shown because of large systematic errors in the multipole decomposition.

Fig.18. Gamow Teller quenching factors for (p,n), (p,p′) and (n,p) reactions on ^{54}Fe and various theoretical models described in the main text.

Fig.19. The S=0 cross sections at five angles obtained after subtraction of the S=1 cross sections.

Fig.20. The S=0, L=1 (bottom) and S=0, L=2 (top) strengths in ^{54}Fe(p,p′) expressed as fractions of the respective energy weighted sum rules.

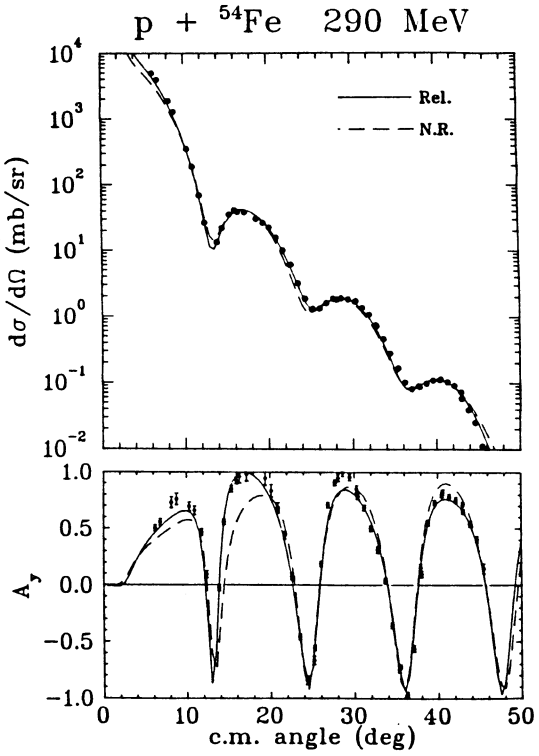

Fig. 1

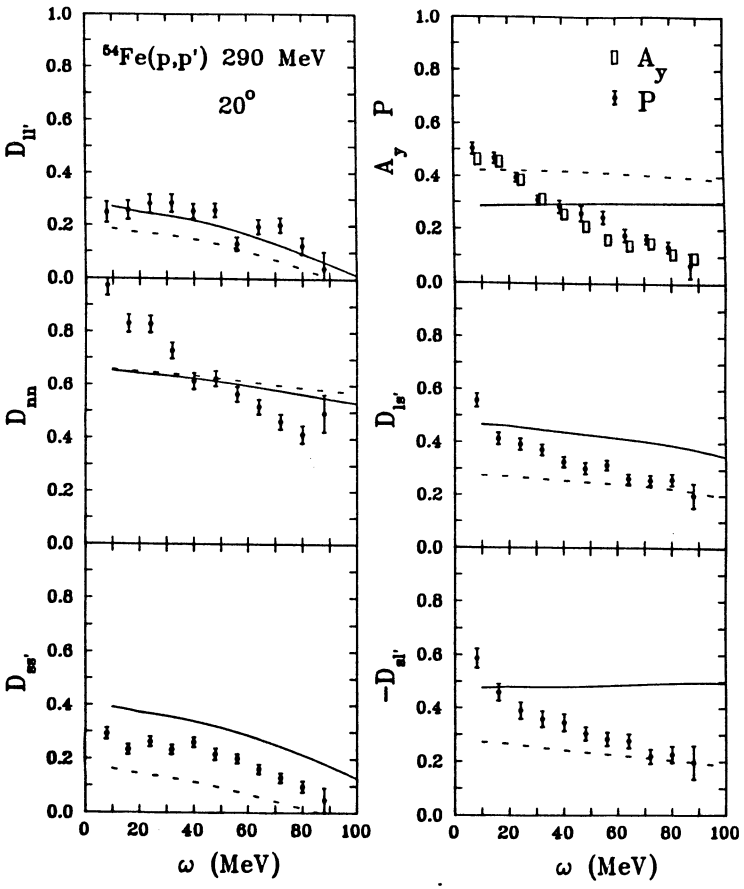

Fig. 2

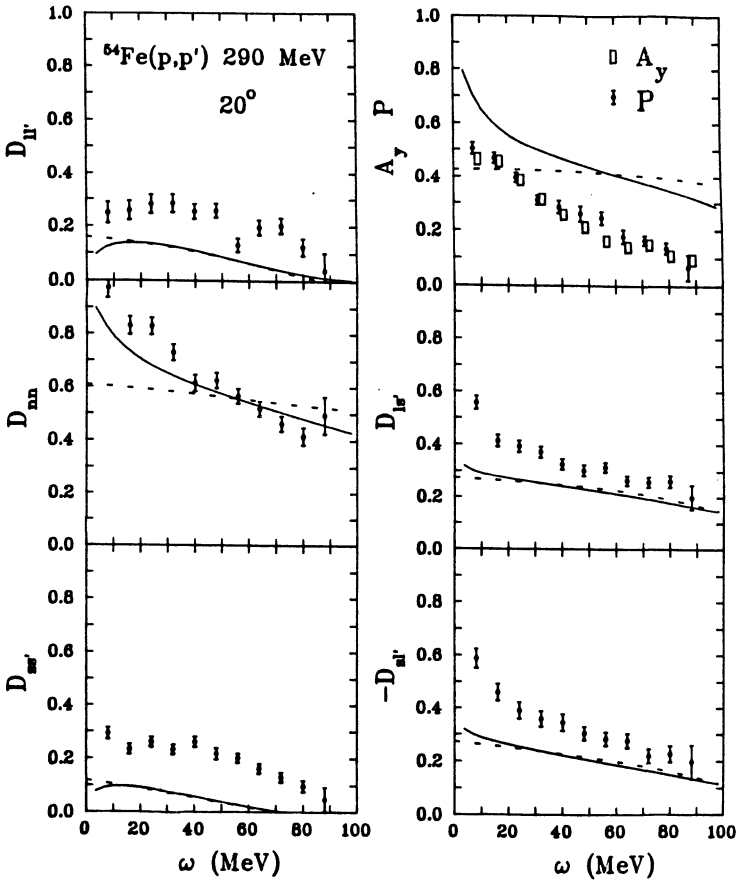

Fig. 3

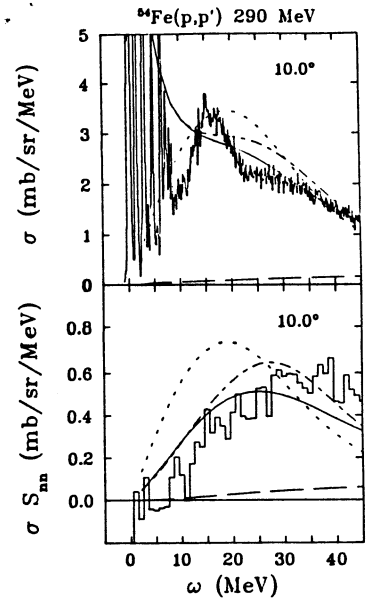

Fig. 4

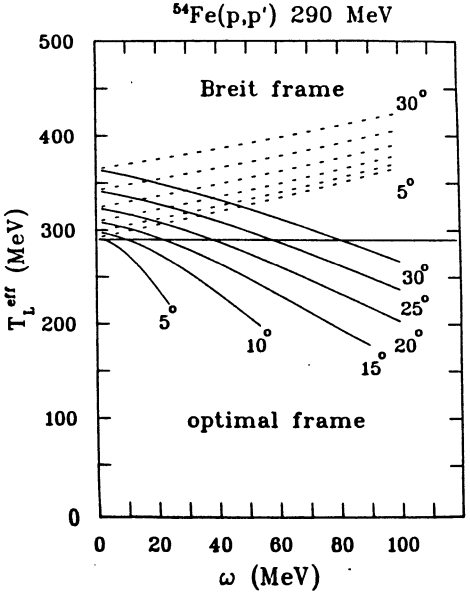

Fig. 5

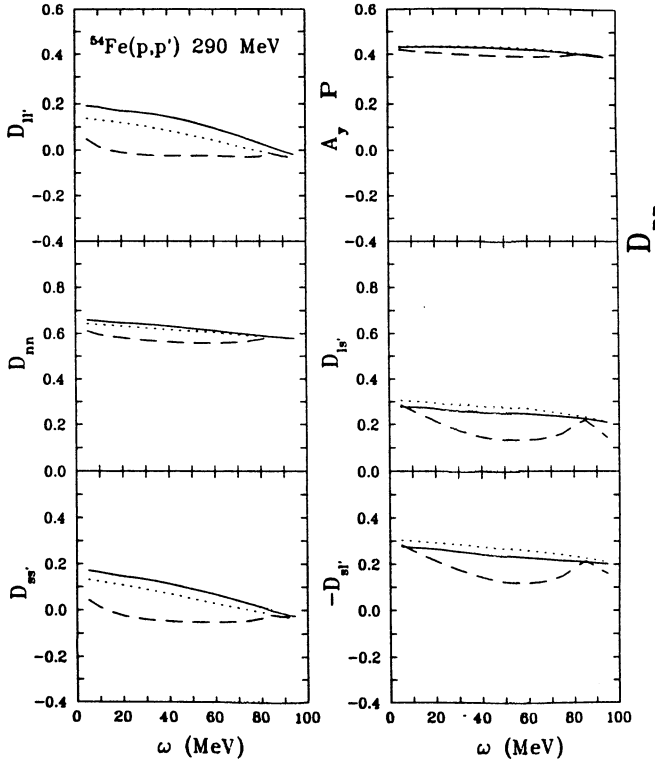

Fig. 6

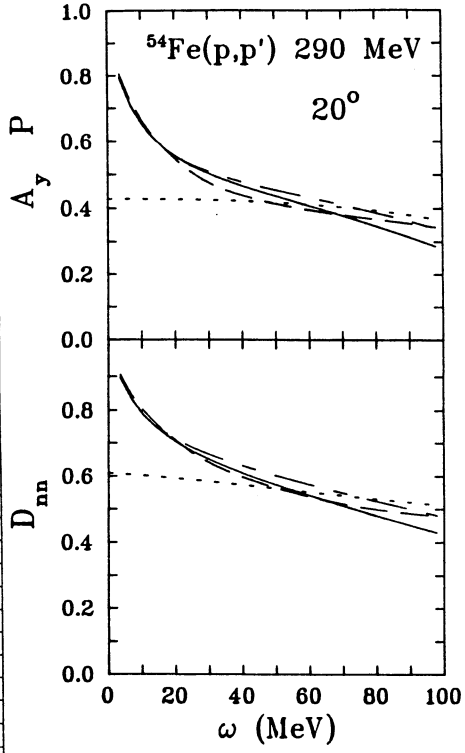

Fig. 7

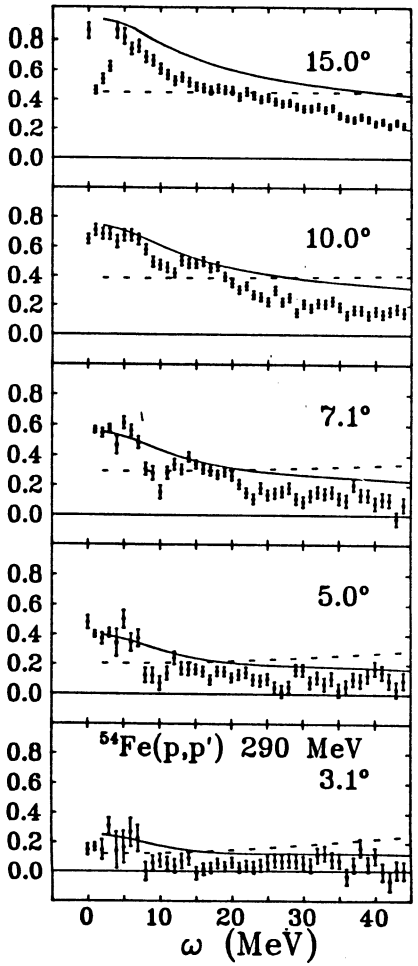

Fig. 8

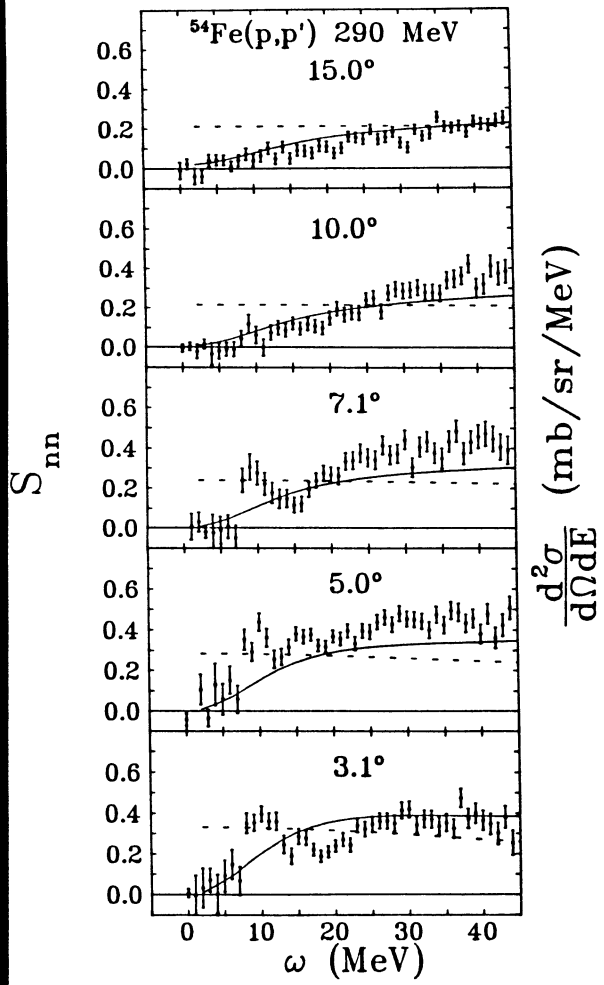

Fig. 9

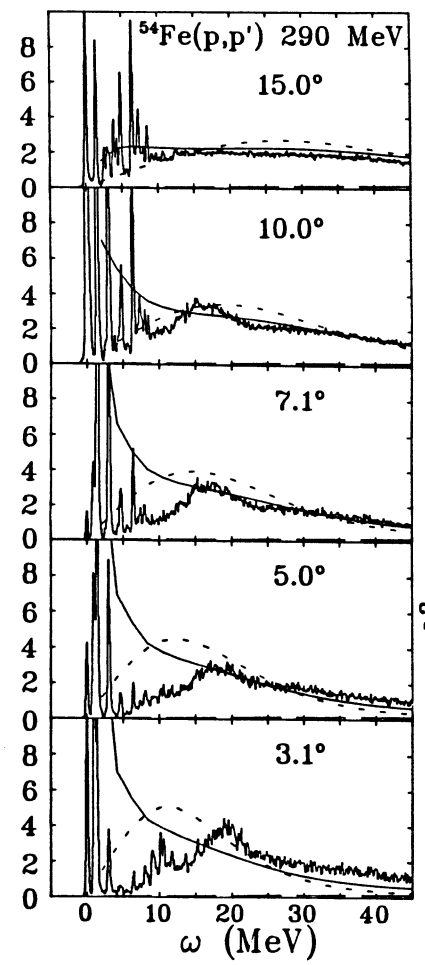

Fig. 10

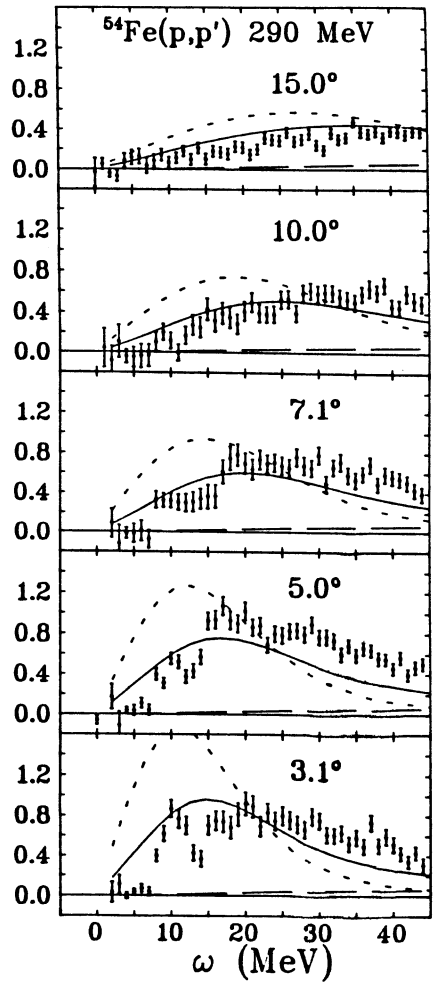

Fig. 11

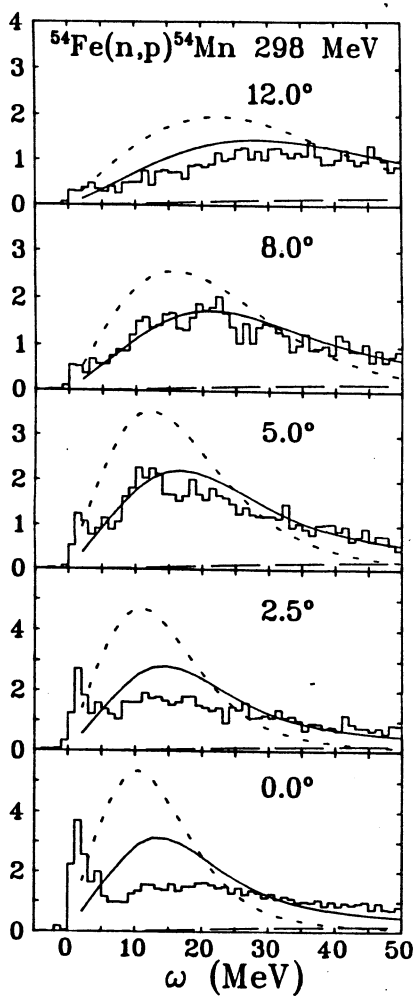

Fig. 12

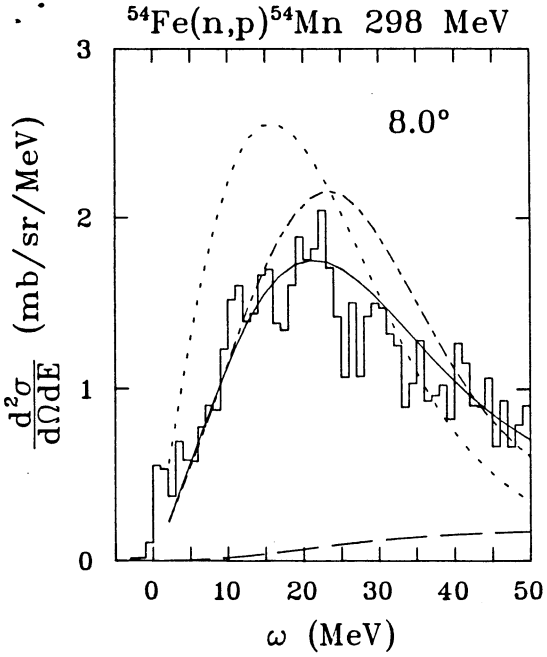

Fig. 13

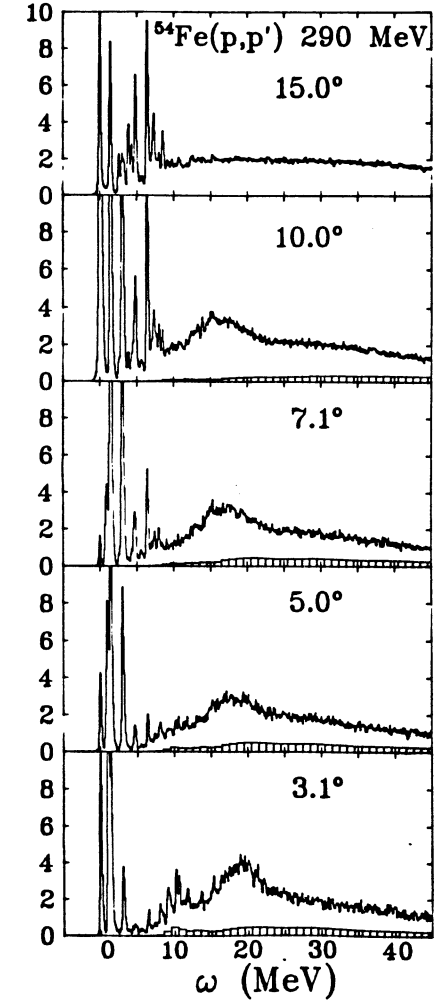

Fig. 14

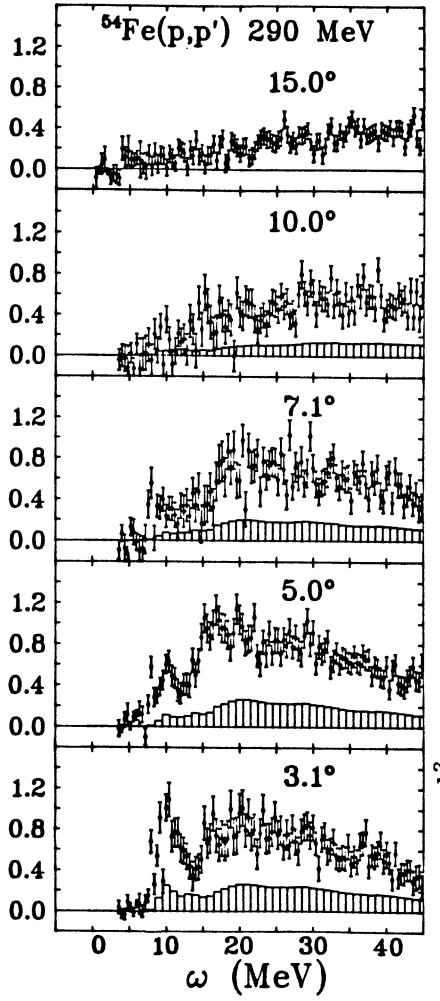

Fig. 15

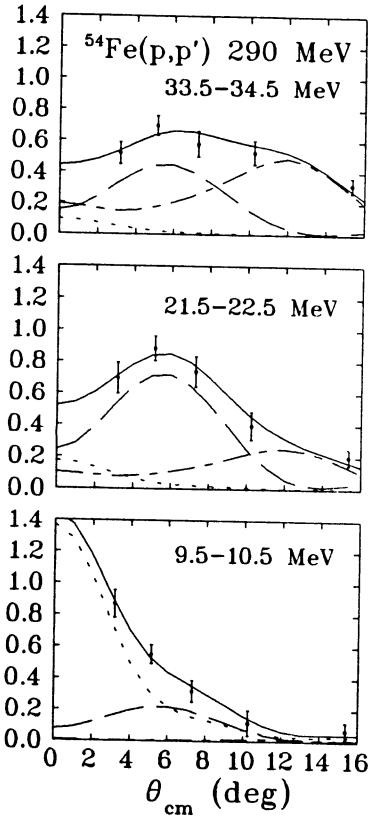

Fig. 16

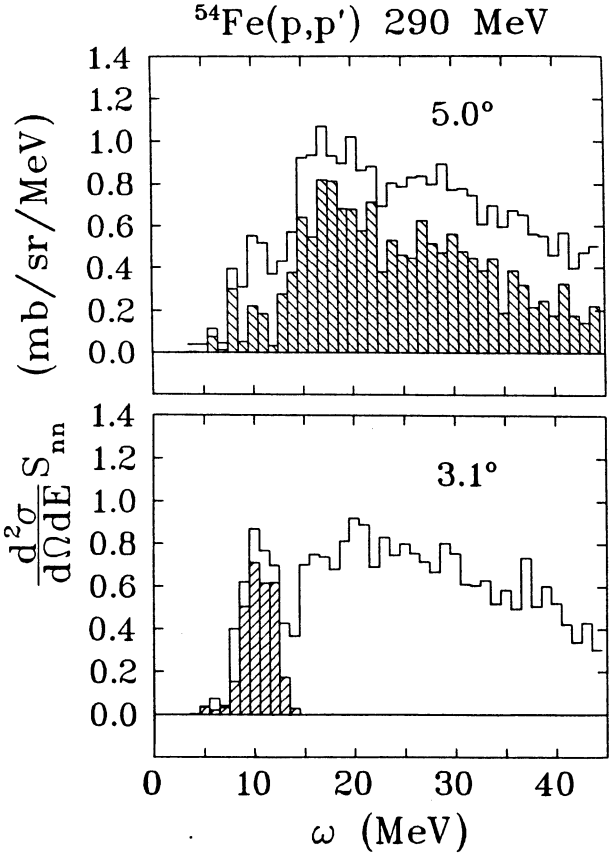

Fig. 17

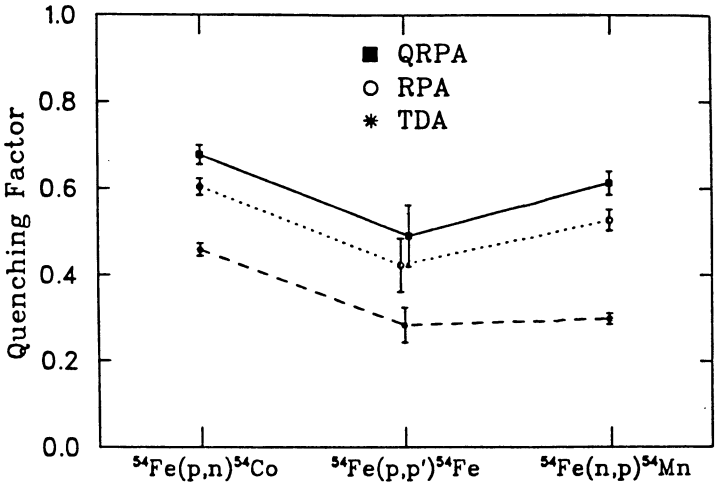

Fig. 18

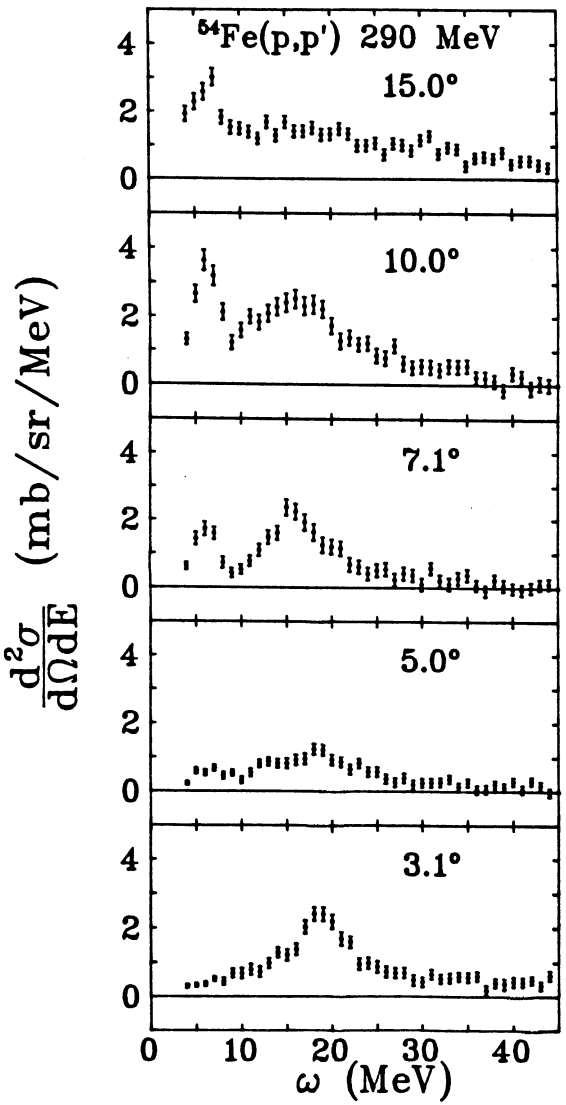

Fig. 19

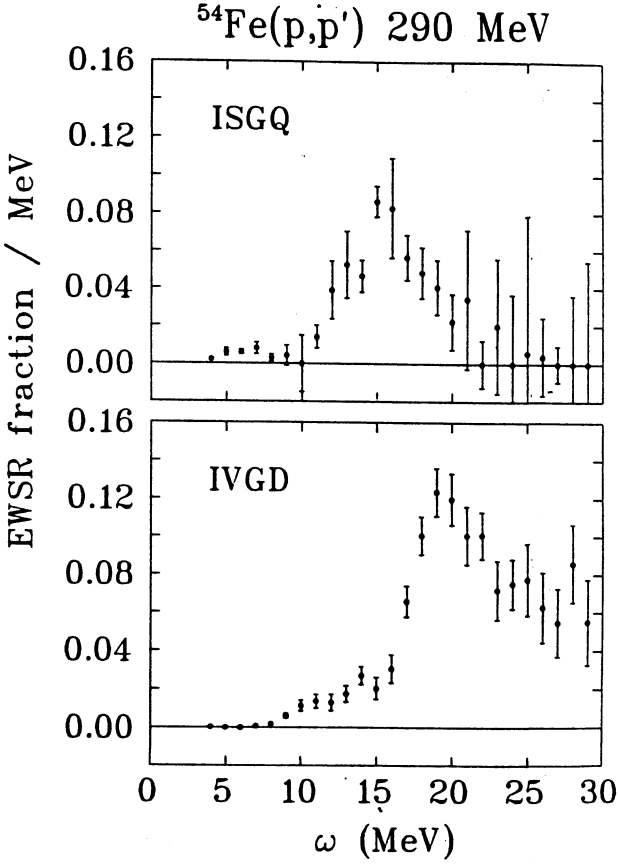

Fig. 20